DTRA-TR-01-18

TECHNICAL REPORT

Infrasound Modeling Using Soviet Explosion Data and Instrument Design Criteria from Experiments and Simulations

Approved for public release; distribution is unlimited.

February 2006

DSWA 01-97-C-0129

Jeffry L. Stevens, et al.,

Prepared by:
Titan Pulse Sciences Division
2700 Merced St.
San Leandro, CA 94577-0599

20060412066

DESTRUCTION NOTICE

4. TITLE AND SUBTITLE Infrasound Modeling Using Soviet Explosion Data and Instrument Design Criteria from Experiments and Simulations	5. FUNDING NUMBERS C-DSWA 01-97-C-0129 PE-RDT&E PR-CD TA-CD WU-DH64928
6. AUTHOR(S) Jeffry L. Stevens, David A. Adams, G. Eli Baker, Heming Xu, John R. Murphy, Igor Divnov, and Vadim N. Bourchik	

7. PERFORMING ORGANIZATION NAME(S) AND ADDRESS(ES) Titan Pulse Sciences Division 2700 Merced St., San Leandro, CA 94577-0599	8. PERFORMING ORGANIZATION REPORT NUMBER MTSD-DTR-00-16619
9. SPONSORING/MONITORING AGENCY NAME(S) AND ADDRESS(ES) Defense Threat Reduction Agency 8725 John J. Kingman Road, MS 6201 Fort Belvoir, VA 22060-6201 TDND/Cartledge	10. SPONSORING/MONITORING AGENCY REPORT NUMBER DTRA-TR-01-18

11. SUPPLEMENTARY NOTES
This work was sponsored by the Defense Threat Reduction Agency under RDT&E RMC code B 4613 D CD CD 64928 5P50 A 25904D.

12a. DISTRIBUTION/AVAILABILITY STATEMENT Approved for public release; distribution is unlimited.	12b. DISTRIBUTION CODE

13. ABSTRACT *(Maximum 200 words)*

This report covers two major topics: evaluation of International Monitoring System (IMS) network performance using data from historic Soviet nuclear tests and analysis of infrasound instrumentation design. The Institute for the Dynamics of the Geospheres has digitized 220 infrasound waveforms from 22 atmospheric nuclear tests conducted in 1961. We compare measurements from this data set with infrasound scaling and attenuation relations and find best agreement with a relation developed by Los Alamos National Laboratory. We estimate that the IMS detection threshold is approximately one kiloton worldwide, but higher in broad ocean areas and lower in continental regions. Network simulations would be improved by including the non-Gaussian character of infrasound noise distributions.

Infrasound recording instruments use an array of pipes connected to a central manifold to spatially filter random pressure fluctuations and enhance the signal-to-noise ratio (S/N). We present a rapid, accurate method of estimating any pipe configuration's response, and calculate the response of proposed IMS pipe configurations. The most important design criterion for enhancing S/N is sufficient spatial sampling, which is improved with larger pipe array dimensions. Open-ended pipes are preferable because they have flatter phase responses, and they have flat amplitude responses, while closed-ended pipes act as lowpass filters.

14. SUBJECT TERMS Infrasound Attenuation Instrument Scaling Relation Atmospheric Explosion			15. NUMBER OF PAGES 72
			16. PRICE CODE

17. SECURITY CLASSIFICATION OF REPORT UNCLASSIFIED	18. SECURITY CLASSIFICATION OF THIS PAGE UNCLASSIFIED	19. SECURITY CLASSIFICATION OF ABSTRACT UNCLASSIFIED	20. LIMITATION OF ABSTRACT SAR

CLASSIFIED BY:

N/A since Unclassified

DECLASSIFIED BY:

N/A since Unclassified

7. PERFORMING ORGANIZATION NAME(S) AND ADDRESS(ES) (contintued)

The Institute for Dynamics of Geospheres
 Of the Academy of Sciences of Russia
Leninsky Prospect, 38
Korpus 6
Moscow, Russia

Conversion Table

Conversion factors for U.S. Customary to metric (SI) units of measurement

MULTIPLY → TO GET ←	BY → BY ←	TO GET / DIVIDE
angstrom	1.000 000 X E -10	meters (m)
atmosphere (normal)	1.013 25 X E +2	kilo pascal (kPa)
bar	1.000 000 X E +2	kilo pascal (kPa)
barn	1.000 000 X E -28	meter^2 (m^2)
British thermal unit (thermochemical)	1.054 350 X E +3	joule (J)
calorie (thermochemical)	4.184 000	joule (J)
cal (thermochemical)/cm^2	4.184 000 X E -2	mega joule/m^2 (MJ/m^2)
curie	3.700 000 C E +1	* giga becquerel (GBq)
degree (angle)	1.745 329 X E -2	radian (rad)
degree Fahrenheit	$t_k = (t°f + 459.67)/1.8$	degree kelvin (K)
electron volt	1.602 19 X E -19	joule (J)
erg	1.000 000 X E -7	joule (J)
erg/second	1.000 000 X E -7	watt (W)
foot	3.048 000 X E -1	meter (m)
foot-pound-force	1.355 818	joule (J)
gallon (U.S. liquid)	3.785 412 X E -3	meter^3 (m^3)
inch	2.540 000 X E -2	meter (m)
jerk	1.000 000 X E +9	joule (J)
joule/kilogram (J/kg) (radiation dose absorbed)	1.000 000	Gray (Gy)
kilotons	4.183	terajoules
kip (1000 lbf)	4.448 222 X E +3	newton (N)
kip/inch^2 (ksi)	6.894 757 X E +3	kilo pascal (kPa)
ktap	1.000 000 X E +2	newton-second/m^2 (N-s/m^2)
micron	1.000 000 X E -6	meter (m)
mil	2.540 000 X E -5	meter (m)
mile(international)	1.609 344 X E +3	meter (m)
ounce	2.834 952 X E -2	kilogram (kg)
pound-force (lbs avoirdupois)	4.448 222	newton (N)
pound-force inch	1.129 848 X E -1	newton-meter (N•m)
pound-force/inch	1.751 268 X E +2	newton/meter (N/m)
pound-force/foot^2	4.788 026 X E -2	kilo pascal (kPa)
pound-force/inch^2 (psi)	6.894 757	kilo pascal (kPa)
pound-mass (lbm avoirdupois)	4.535 924 X E -1	kilogram (kg)
pound-force/foot^2 (moment of inertia)	4.214 011 X E -2	kilogram-meter^2 (kg•m^2)
pound-mass/foot^3	1.601 846 X E +1	kilogram-meter^3 (kg•m^3)
rad (radiation dose absorbed)	1.000 000 X E -2	** Gray (Gy)
roentgen	2.579 760 X E -4	coulomb/kilogram (C/kg)
shake	1.000 000 X E -8	second (s)
slug	1.459 390 X E +1	kilogram (kg)
torr (mm HG, 0°C)	1.333 22 X E -1	kilo pascal (kPa)

* The becquerel (Bq) is the SI unit of radioactivity; 1Bq = 1 event/s.
** The Gray (GY) is the SI unit of absorbed radiation.

A more complete listing of conversions may be found in "Metric Practice Guide E 380-74,"
American Society for Testing and Materials.

Table of Contents

Table of Contents (Continued)

Figures

Tables

Acknowledgments

Section 1
Introduction

This report covers two major topics:

1. modeling of infrasound signals from atmospheric explosions and evaluation of International Monitoring System network performance using data from historic Soviet nuclear tests and other infrasound data sources; and

2. analysis of infrasound instrumentation through a program of experimentation and theoretical modeling.

The Institute for the Dynamics of the Geospheres (IDG) in Moscow, Russia, has an archive of infrasound recordings from Soviet atmospheric nuclear tests that were conducted in 1957 and 1961. IDG has digitized a total of 220 infrasound waveforms from 22 atmospheric nuclear tests. Two events were high altitude explosions at Kapoustin Yar, 8 others were at the Shagan River Test Site, and the other 12 were at Novaya Zemlya. 138 of the waveforms have measurable, unclipped signals, known instrument responses, yields, and calibrations. We have been modeling this data in two ways: first, by using the data to place constraints on infrasound scaling relations; and second, by numerical modeling of the infrasound signals. Scaling relations estimate the pressure as a function of yield and range. Several scaling relations exist in the literature, and the differences between them lead to large differences in estimates of the detection threshold of the International Monitoring System (IMS). We find that the data is in best agreement with a scaling and attenuation relation developed by Los Alamos National Laboratory (LANL) which can be written as $\log P = 3.37 + 0.68 \log W - 1.36 \log R$ where P is zero to peak pressure amplitude in Pascals, W is the yield in kilotons, and R is the source to receiver distance in kilometers.

IMS network detection capability is predicted using the network simulation programs NetSim and XNICE. NetSim uses joint probabilities together with a scaling relation to calculate the detection threshold. XNICE has the additional capability of estimating the detection threshold for non-Gaussian noise distributions. We find that IMS noise levels have a time-dependent and non-Gaussian distribution. The noise is characterized by a fairly well-defined minimum level, but highly variable maxima. The two-station 90% probability IMS detection threshold is found to be about one kiloton with higher thresholds in ocean regions and lower thresholds on land.

A typical infrasound recording instrument uses an array of pipes connected to a central manifold to spatially filter random pressure fluctuations along the ground and so enhance the signal-to-noise ratio (S/N). We present a rapid, accurate, method of estimating the performance of any pipe configuration used for infrasound recording. We first describe experimental work that provides the physical basis for simulations and permits estimation of parameter values. We then describe the propagator method used for the calculations. The performance of a pipe array depends on the character of the noise, and so meaningful modeling of infrasound pipe array performance hinges on accurate knowledge of the temporal and spatial distribution of pressure fluctuations over the array. We discuss the physical basis for the noise model, and limitations imposed by necessary simplifications. We present the amplitude and phase responses, and their sensitivities to different parameters, of two different types of pipes used to construct the arrays: closed-ended pipes with acoustic inlets along their lengths versus open ended, otherwise impermeable pipes. Finally, we

simulate the S/N enhancement for six different pipe configurations that have been considered for the IMS infrasound stations, and discuss the results' implications for instrument design.

We find that open-ended pipes are preferred over closed-ended pipes with high impedance acoustic inlets. The open-ended pipes have essentially flat amplitude responses, while the closed-ended pipes act as lowpass filters. The open-ended pipes also have flat phase responses, while the phase responses of the closed-ended pipes vary much more across the spectrum of interest. The most important design criterion for enhancing S/N is having sufficient spatial sampling. Extra ports, however, provide no advantage if spaced more closely than the noise correlation length. All configurations performed well, and similarly, at high frequencies, as the high frequency noise has the least spatial correlation. The differences in performance are very significant at the lower frequencies. The two 70 m diameter configurations provide the best performance in our simulations of S/N enhancement, and their performances were nearly identical even though one had 144 ports and the other had only 96. The 18 m diameter configuration performed the worst at low frequency. The most important step that can be taken now to improve instrument performance is to obtain, and utilize in such modeling, more complete and accurate noise models.

Section 2
Infrasound Scaling and Attenuation Relations and IMS Detection Capability

The International Monitoring System (IMS) specified by the Comprehensive Nuclear-Test-Ban Treaty (CTBT) will include sixty infrasound stations designed to detect atmospheric nuclear explosions (Figure 1). A design goal is that the system be able to detect and locate explosions as small as one kiloton anywhere in the world. In order to estimate the capability of the infrasound network, it is necessary to be able to predict the amplitude of an infrasound signal at any location, and to evaluate whether the signal would be detectable above noise levels at the recording stations. Scaling and attenuation relations are empirical and/or theoretical equations that relate the amplitude and period of infrasound signals to the explosion yield and source to receiver distance. Several different relations have been developed based on theoretical infrasound modeling, and on recordings of atmospheric nuclear and chemical explosions. The different scaling relations, however, imply very different detection threshold levels. In the following section we review the different relations and their implications for detection thresholds.
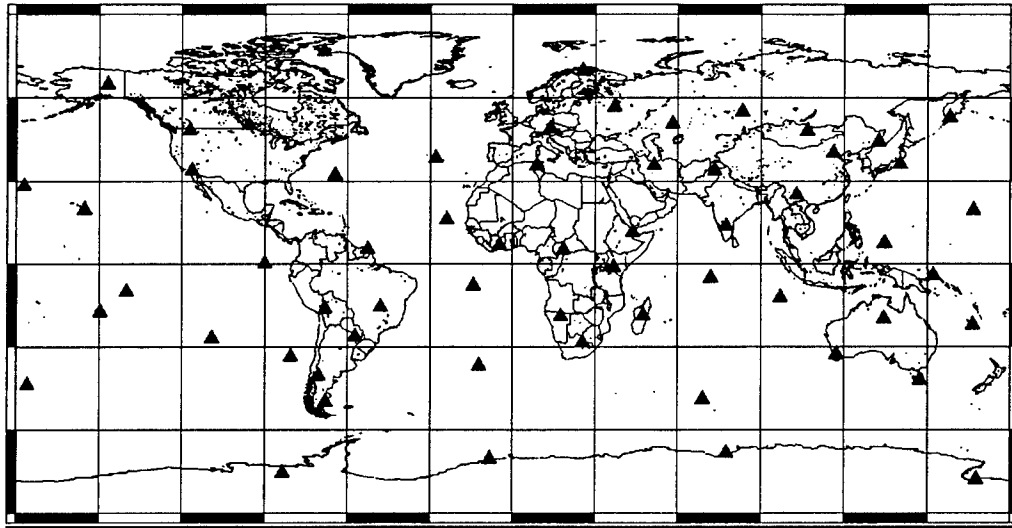
Figure 1. Stations of the planned IMS infrasound network.

2.1 Infrasound Scaling and Attenuation Relations.

Pierce and Posey (1971) developed a solution for the excitation of the Lamb edge mode as an approximation for infrasound signals generated by atmospheric tests. They showed that this relatively simple approximation gave waveforms that agreed well with the first few cycles of observed waveforms from multi-megaton nuclear tests. From this they developed the relation between the yield W in kilotons, zero to peak pressure P in Pascals, the period of the first cycle of the waveform T, and the angular distance Δ given by:

$$W = 0.494 P(\sin \Delta)^{\frac{1}{2}} H_s (cT)^{3/2} \tag{1}$$

where c is the sound speed, H_s is the atmospheric scale height $c^2/\gamma g$, where γ is the adiabatic expansion constant, approximately 1.4 for air, and g is the acceleration of gravity. Posey and Pierce (1971) showed that this relation agreed well with a data set of observations of pressure and period measurements from large atmospheric nuclear explosions.

The derivation of Equation 1 uses the approximation that the period being measured is much longer than the source duration. Pierce and Posey estimated the source duration to be approximately $T_s = 0.33W^{1/3}$ seconds, which is only about 13 seconds even for a 58 megaton explosion, and therefore always much less than the measured infrasound period. This approximation has the effect of making period independent of yield and proportional to the cube root of distance. For the typical sound velocity (.318 km/sec) and scale height (8 km) referenced in the paper, the period of the first cycle of the Lamb wave can be written as

$$T = 13.4R^{1/3} \tag{2}$$

where R is the source to receiver distance in kilometers and T is in seconds. Equation 2 can then be combined with equation 1 to give

$$W = 34.8PR^{1/2}(\sin\Delta)^{1/2} \tag{3}$$

The pressure is therefore predicted to be proportional to yield at a fixed distance and to decrease approximately inversely with distance. As can be seen from the data in the following section, these predictions are inconsistent with the data which scales much more slowly than linearly with yield and exhibits a clear frequency dependence with yield.

Equation 1 has been widely used (McKisic, 1997) and turns out to be in good agreement with the data when the observed period is used, even though the usage is inconsistent with the derivation of equation 1. Blandford and Clauter (1995) modified equation 1 by assuming that the period T is proportional to the cube root of yield and independent of distance. From this it follows that pressure is proportional to the square root of yield and decays as the square root of distance from the source. Blandford and Clauter (1995) used the square root of distance decay at distances less than 20 degrees, but modified the attenuation relation to have an exponential form at distances greater than 20 degrees to match the data set of Wexler and Hass (1962). Using a larger data set, keeping the same yield scaling, but modifying the attenuation relation, Clauter and Blandford (1998) derived the relation:

$$\log P = 0.92 + 0.5\log W - 1.47\log\Delta \tag{4}$$

where Δ is the source to receiver distance in degrees, W is the yield in kilotons, and P is the zero to peak pressure amplitude in Pascals. They showed that this relation was consistent with a historical data set of nuclear and chemical explosions.

Whitaker (1995) derived the following relation based on wind-corrected infrasound measurements from Los Alamos chemical explosions:

$$P_c = 2.35x10^3(R/W^{1/2})^{-1.36} \tag{5}$$

4

where P_c is the wind corrected zero to peak pressure in Pascals, R is the source to receiver distance in kilometers, and W is the yield in kilotons (the original reference stated that yield is in tons, but should be kilotons (Whitaker, personal communication)). The wind correction applied in equation 5 is

$$P_c = 10^{-0.019v} P \qquad (6)$$

where v is the component of the stratospheric wind velocity in meters/second in the direction of wave motion and P is the measured pressure.

Russian scientists at IDG have used the following relationships to make approximate yield estimates:

$$P_m = k_p W^{1/3} / R \qquad (7)$$

$$T = k_T W^{1/3} / R \qquad (8)$$

$$\omega_m = k_\omega / W^{1/3} \qquad (9)$$

where P_m is the zero to peak pressure in Pascals, T is the signal duration from the first arrival to the moment when the signal degrades to noise level, and 90% of the signal energy is contained in the frequency band below angular frequency ω_m. The three constants are empirically determined and are given in Table 1.

Table 1. Russian scaling constants

	k_p Pa-km/kt$^{1/3}$	k_T s/kt$^{1/3}$km	k_m kt$^{1/3}$/s
Downwind	2000	0.050	1.6
Perpendicular to wind	1000	0.025	1.2

The equations above can be written in a consistent format as:

$$\log P = -1.54 + \log W - 0.5 \log(R \sin \Delta) \qquad \text{Pierce and Posey (1971)} \qquad (10)$$

$$\log P = 0.92 + 0.5 \log W - 1.47 \log \Delta \qquad \text{AFTAC (Clauter and Blandford, 1998)} \qquad (11)$$

$$\log P = 3.37 + 0.68 \log W - 1.36 \log R \qquad \text{LANL (Whitaker, 1995)} \qquad (12)$$

$$\log P = 3.00 + 0.33 \log W - \log R \qquad \text{Russian – Crosswind} \qquad (13)$$

$$\log P = 3.30 + 0.33 \log W - \log R \qquad \text{Russian – Downwind} \qquad (14)$$

where P is zero to peak pressure in Pascals, W is yield in kilotons, R is distance in kilometers, and Δ is distance in degrees.

These scaling relations have very different implications for the infrasound detection threshold. Yield estimates for the threshold pressure level differ by several orders of magnitude, even though each relation was constrained by some infrasound data set. Table 2 shows the calculated

5

yield at a nominal detection threshold of 0.1 Pascal for each of the scaling relations. The most important factor is the exponent in the pressure/yield relation. With the Pierce/Posey relation, which has a yield exponent of 1, pressure drops off much more rapidly with yield than with the other relations leading to a very high threshold level. The 0.33 yield exponent in the Russian relations, however, implies a very slow decrease in pressure with yield and leads to very low threshold levels. The Whitaker and Clauter/Blandford relations, which have yield exponents of 0.68 and 0.5, respectively, predict intermediate threshold levels.

Table 2. Detection capability for a nominal detection threshold of 0.1 Pascal. The table shows yield in kilotons for each scaling relation and source to receiver distances from 10-60 degrees.

	10	20	30	40	50	60
Clauter/Blandford	0.13	0.97	3.2	7.4	14	24
Whitaker	0.46	1.8	4.2	7.4	11	17
Russia Crosswind	0.0014	0.01	0.037	0.088	0.17	0.30
Russia Downwind	0.0002	0.0014	0.0046	0.011	0.02	0.037
Pierce/Posey	47	93	140	180	220	260

2.2 Soviet Infrasound Data.

IDG has an archive of approximately 300 recordings from 34 Soviet atmospheric nuclear tests that were conducted in 1957 and 1961. 20 of these explosions were located at the Novaya Zemlya test site, 12 at Semipalatinsk, and 2 at Kapoustin Yar (see Figure 2). Of these, 220 recordings from 22 of the tests recorded at stations from 1000 to 5000 km were found to be of adequate quality for digitization. The yields of these tests range from 0.4 KT to 58 MT. The data set includes two high altitude explosions and the largest (58 megaton) atmospheric explosion ever detonated. The explosions corresponding to this data set are listed in Table 3. The number of records listed in the table is the total number of records digitized for each event.
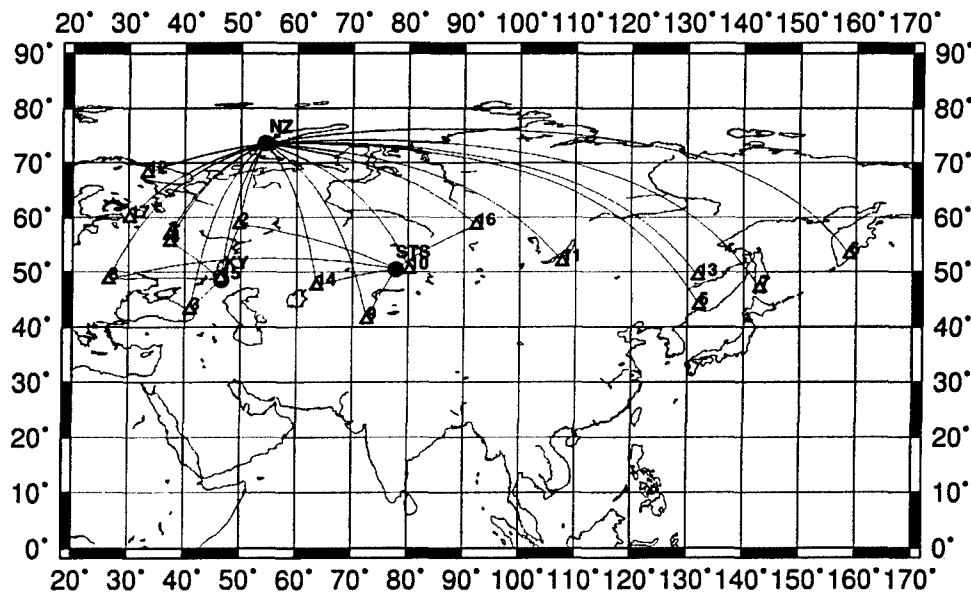
Figure 2. Stations recording infrasound signals from atmospheric explosions at three Soviet nuclear test sites Semipalatinsk (STS), Kapoustin Yar (KY), and Novaya Zemlya (NZ).

Table 3. Soviet atmospheric nuclear explosions and the number of records for each event that have been digitized by IDG. STS is the Semipalatinsk test site, KY is Kapoustin Yar, and NZ is Novaya Zemlya.

Test Site	Explosion Number	Date	Time (Moscow)	Latitude	Longitude	Height of Burst (m)	Yield (KT)	Number Records
STS	088	1961/09/04	08:00:27	50.45	77.74	725	9	2
STS	089	1961/09/05	09:00:05	50.45	77.74	500	16	3
KY	091	1961/09/06		48.45	44.30	22700	11	6
NZ	095	1961/09/10	12:00:14	73.52	54.30	2000	2700	23
NZ	099	1961/09/12	13:08:00	73.52	54.30	1190	1150	23
NZ	102	1961/09/14	12:56:16	73.52	54.3	1700	1200	17
STS	103	1961/09/14	08:59:59.4	50.35	77.82	0.5	0.4	1
NZ	111	1961/09/20	11:12:12	73.52	54.30	1600	450-2000[1]	6
STS	112	1961/09/21	17:01:01.6	50.33	77.70	110	0.8	2
NZ	113	1961/09/22	11:11:00	73.52	54.30	1300	260	4
STS	114	1961/09/26	10:01:19.8	50.45	77.75	665	1.2	2
NZ	116	1961/10/02	13:30:50	73.92	54.55	1500	250	13
STS	117	1961/10/04	10:01:19.9	50.44	77.76	605	13	1
KY	119	1961/10/06		48.45	44.30	41300	40	4
NZ	120	1961/10/06	10:00:08	73.52	54.30	2700	4000	20
STS	123	1961/10/17	10:00:00.8	50.45	77.75	505	6.6	2
STS	124	1961/10/19	08:30:42.6	50.45	77.73	710	10	2
NZ	125	1961/10/20	11:07:03	73.52	54.30	1000[2]	1450	17
NZ	126	1961/10/23	11:31:22	73.5	54.3	3500	12500	21
NZ	128	1961/10/25	11:31:05	73.52	54.3	1450	300	10
NZ	133	1961/10/30	11:33:27	73.52	54.30	4000	58000	21
NZ	147	1961/11/04	10:20:23	73.5	54.3	1750	150-1500	20

Seventeen stations recorded data from these tests. The stations are listed in Table 4 and Figure 2 shows the paths from each event to each station in the data set. Absolute times are not known for any of the waveforms. Data were recorded on instruments with varying low and high pass filters. Figure 3 shows the response of the three major instrument types. IDG has put considerable effort into identifying the instrument parameters that were in use at each of the recording stations. The instrument parameters are defined and described for each station in Appendix A. Appendix B lists the instrument parameters for each waveform together with IDG measurements of a number of parameters.

---

[1] Yield information varies. 2000 kt was used in the analysis in this report. IDG used 450 kt in Appendix B.
[2] IDG estimate.

Амплитудно-частотные характеристики регистрирующей аппаратуры

1 — ЖБС
2 — СКМб-58
3 — СКМб-П
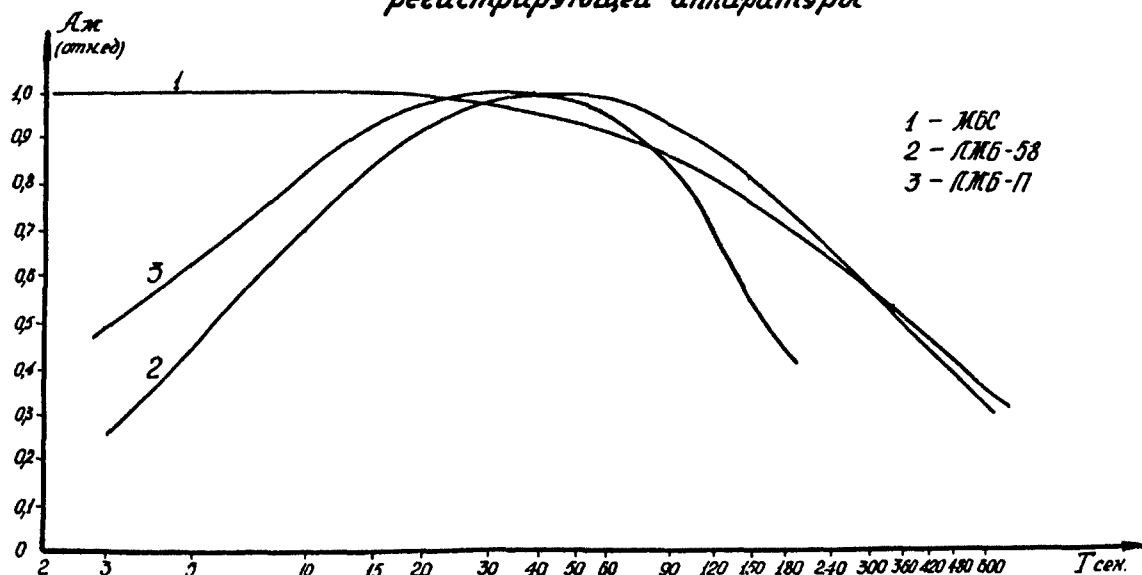
Figure 3. Three major instrument types used for recording infrasound data.

Table 4. Stations recording Soviet atmospheric tests.

Station Num.	Station Name	Latitude	Longitude	Novaya Zemlya distance (km)	Semipalatinsk distance (km)	Kapoustin Yar distance (km)
1	Dubna	56.7	37.3	2200	2700	900
2	Kirov	58.6	49.7	1700	2100	1100
3	Esheri	43.1	40.9	3500	2900	800
4	Podolsk	55.5	37.3	2200	2700	900
5	Oussouriysk	43.9	132.0	5000	4100	6300
6	Petropavlovsk	53.1	158.8	4850	5300	7100
7	Yuzno-Sakhalinsk	47.0	142.8	5000	4600	6700
8	Zvanets	48.5	26.4	3150	3650	1400
9	Mayly-say	41.3	72.5	3800	1140	2250
10	Semipalatinsk	50.4	80.2	2850	-	2500
11	Baykal	51.8	107.6	3450	2000	4250
12	Olenegorsk	68.1	33.3	1000	3100	2300
13	Kooldour	49.2	131.8	4450	3800	5900
14	Kazakhstan	47.5	63.5	2950	1100	1250
15	Kap Yar	48.7	46.4	2800	2250	-
16	Yeniseysk	58.5	92.2	2350	1300	3300
17	Leningrad Reg.	59.9	30.2	1850	2800	1650

Some examples of infrasound records are shown in Figure 4. These records are from tests that range from 8 kilotons to 58 megatons in yield. All of these traces were recorded on instrument #2 except those for event 133, which were recorded on instrument #1. The frequency content of the signals changes dramatically over this range.

8
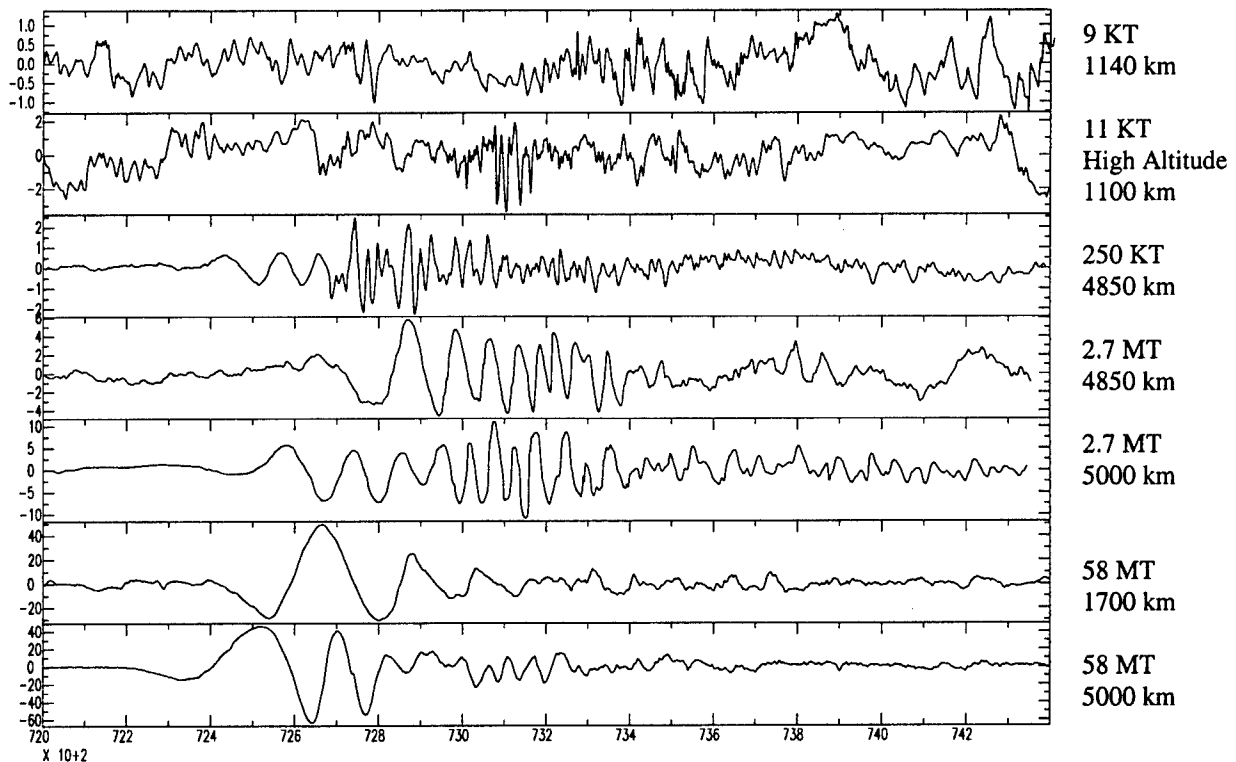
Figure 4. Infrasound signals from Soviet atmospheric tests. The top record is from test 088 at station 9, the second is from the high altitude test 091 at station 2, the third is from the test 116 at station 6, the fourth and fifth are from test 095 at stations 6 and 7, and the last two records are from the test 133 at stations 2 and 7. Amplitudes are in Pascals.

2.3 Measurement of Russian Data.

All of the Russian data were carefully measured in a consistent manner. The data were first filtered to remove long and short period noise outside the frequency band of the data. A Butterworth filter was used with corner frequencies of .01 and .2 Hz for events with yield less than 100 kilotons, .002 and .1 Hz for events with yields between 100 kilotons and 2 megatons, and .001 and .1 Hz for events with yield greater than 2 megatons. The amplitude and period were measured as half the maximum peak to peak amplitude and twice the time difference between the peak and trough, respectively. Measurements were made on both the acoustic wave and the low frequency Lamb wave if possible. Only data with known instrument responses were measured, and a digital correction for the instrument response was made at the observed period. A few signals with apparent calibration errors were not used. The final result is that measurements were made on a total of 133 waveforms. 107 acoustic waves from 17 events and 96 Lamb waves from 9 events were measured.
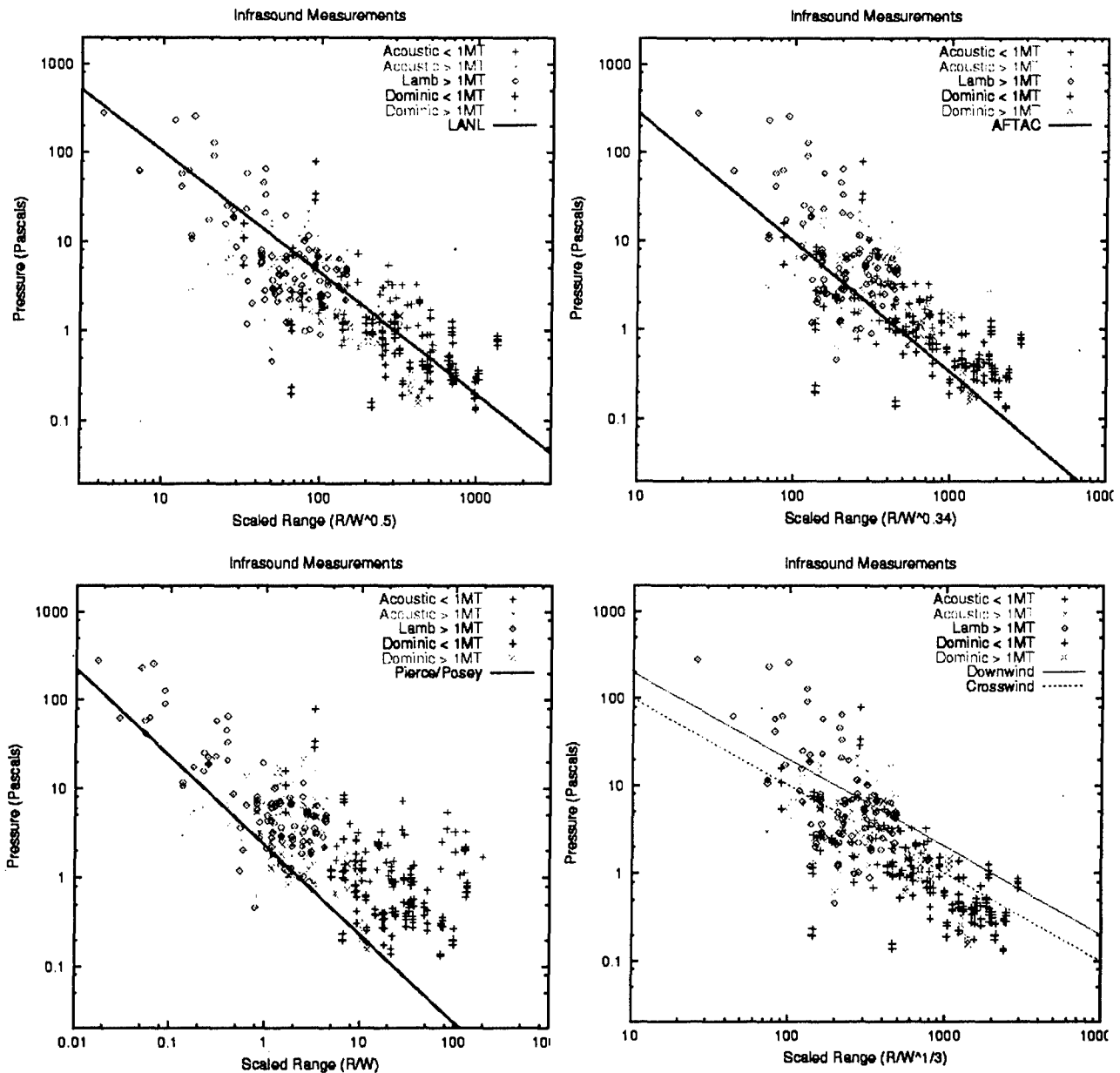
Figure 5. Comparison of Russian data with scaling relations. Top left is the LANL relation (Whitaker) Equation 12, top right the AFTAC relation (Clauter and Blandford) Equation 11, bottom left is the Pierce/Posey relation Equation 10, and bottom right are the Russian relations Equations 13 and 14.

Figure 5 shows a comparison between pressure measurements made from the Russian data and Equations 10-14. Also shown on the figure are measurements from the US Project Dominic tests. It is not possible to put them all on the same plot because the scaling relations have different functional forms. All pressures are zero to peak amplitudes in Pascals. The LANL relation (Equation 12) appears to fit the data very well over the entire scaled range, although there is considerable scatter about the line. The pressure measurements have not been wind corrected. The AFTAC relation (Equation 11) fits the lower yield data quite well. The Pierce/Posey relation (Equation 10) is a fairly good fit to the high yield Lamb wave data, but does not fit the acoustic

wave data, particularly for the lower yield events. The Russian relations (Equations 13-14) also fit the data fairly well with the crosswind equations matching the lower amplitude data and the downwind equations matching the higher amplitude data, however the observed data falls below the predicted curves for larger scaled ranges, and the data points for the largest yield events are well above the curve, while the lower yield events lie below the curve. We conclude from this that the pressure/yield slope of 0.33 used in the Russian relation is too small, and the pressure/yield slope of 1.0 used in the Pierce/Posey relation is too large. The data is consistent with the intermediate slopes of 0.5-0.68 of the AFTAC and LANL relations, with the LANL relation fitting the data over the widest range.
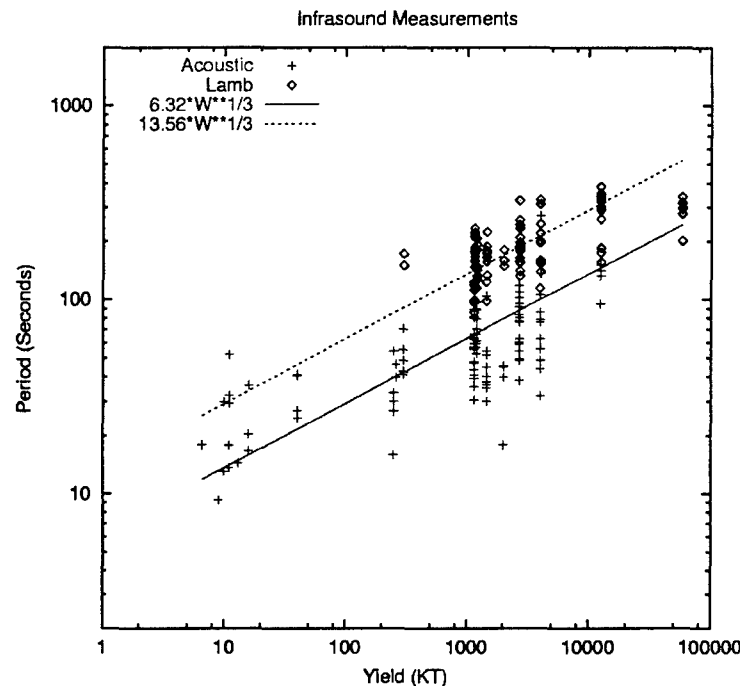
Figure 6. Period vs. explosion yield for all data.

Figure 6 shows the measured period plotted vs. yield for the Russian data, together with lines showing cube root scaling of period with yield with the best fit to the acoustic and Lamb data taken as independent data sets. The cube root scaling approximately fits the data, however there is a large amount of scatter and the slow increase of period with yield would cause considerable uncertainty in a yield estimate based on measured period.

2.4 Infrasound Magnitudes.

In the analysis above, we used a data set of infrasound waveforms from Soviet atmospheric tests ranging in yield from 6 kilotons to 58 megatons to place constraints on infrasound scaling relations and to estimate the detection threshold of the future International Monitoring System. Analysis of 133 waveforms shows that measured pressures are consistent with yield and attenuation scaling relations developed at LANL for HE tests, and also fairly consistent with a scaling relation developed by AFTAC. Because the LANL relation is consistent with data over a

11

very wide yield range, it has recently been adopted as the basis for an infrasound magnitude by the International Data Center (IDC) (Brown, 1999). A magnitude is a useful quantity for giving an estimate of source size that is independent of the distance at which the signal is measured. The magnitude equation is:

$$M_i = \log_{10} P + 1.36 \log_{10} R - 0.019 v \qquad (15)$$

where the last term corrects for wind as discussed earlier. Infrasound magnitudes for the Russian data set (without wind correction), are listed in Table 5. Magnitudes for the acoustic wave and Lamb wave are listed separately. Figure 7 shows M_I plotted vs. Yield for the seven Soviet explosions. Also shown is the LANL relation, Equation 12, rewritten as a magnitude/yield relation:

$$M_I = 0.68 \log W + 3.37 \qquad (16)$$

As can be seen in Figure 7, Equation 16 fits the data over this very wide yield range quite well.

Table 5. Infrasound magnitude for eighteen Soviet explosions.

Test Site	Explosion	M_I Acoustic	$\sigma(M_I)$ Acoustic	Number Acoustic	M_I Lamb	$\sigma(M_I)$ Lamb	Number Lamb
STS	088	4.44		1			
STS	089	4.31	0.05	3			
KY	091	4.53	0.18	5			
NZ	095	5.52	0.26	16	5.50	0.25	16
NZ	099	5.29	0.46	18	5.26	0.37	20
NZ	102	5.29	0.34	13	5.13	0.31	9
NZ	111	5.56	0.40	5	5.42	0.13	3
NZ	113	4.94	0.37	2			
NZ	116	4.98	0.32	6			
STS	117	4.52		1			
KY	119	4.45	0.48	4			
NZ	120	5.38	0.48	11	5.36	0.53	12
STS	123	4.46		1			
STS	124	4.47	0.40	2			
NZ	125	5.43	0.56	9	5.24	0.41	10
NZ	126	5.33	0.35	4	6.15	0.43	14
NZ	128	5.04	0.38	6	4.92	0.38	2
NZ	133				6.69	0.40	10

Infrasound Magnitudes
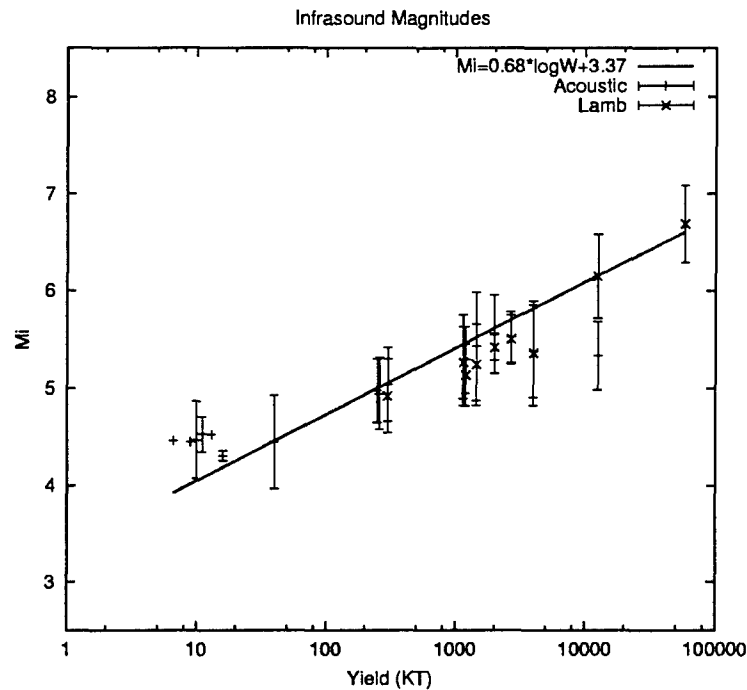
Figure 7. Infrasound magnitude plotted vs. yield for eighteen Soviet explosions.

2.5 Spectral Measurements.

Some additional insight into the scaling laws can be obtained by examining the spectra of arrivals with different yields at the same station. Station 7, at Yuzno-Sakhalinsk, recorded four atmospheric explosions with yields of 250, 1450, 2700, and 58000 kilotons. The spectra of these four arrivals are shown in Figure 8. The shape of the spectra change dramatically over this yield range, with much more low frequency energy at higher yields.
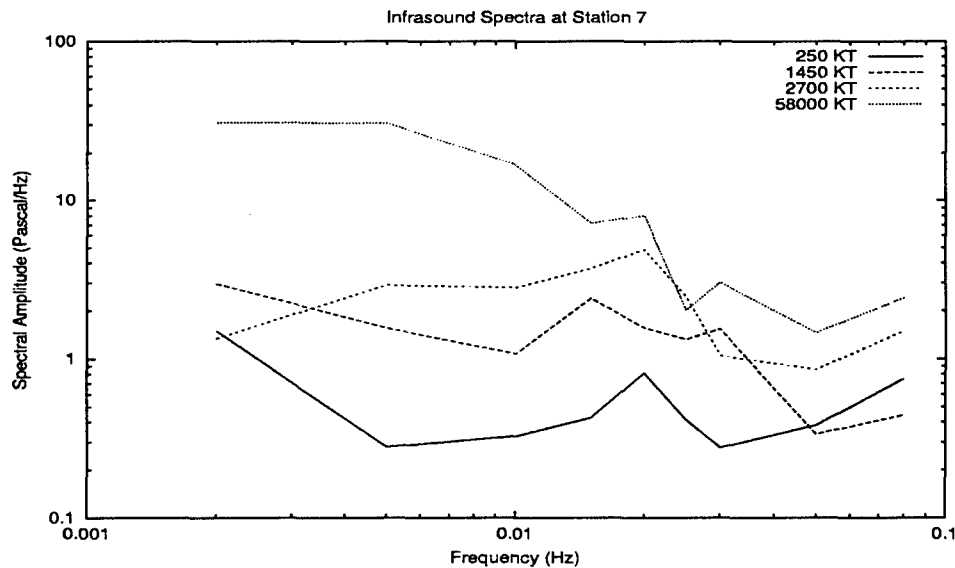
Figure 8. Spectra of four infrasound signals recorded at station 7 with yields of 250, 1450, 2700, and 58000 kilotons.

Figure 9 shows the change in amplitude for three frequencies plotted as a function of yield, showing that the slope of the log amplitude vs. log yield curve changes as a function of frequency. Figure 10 shows the slope of the amplitude vs. yield curve (as shown in Figure 9) plotted as a function of frequency. This figure shows that the slope of the amplitude/yield curve is strongly frequency dependent, and that the slope is close to 1, as in the Pierce/Posey model, at very low frequencies, but declines to approximately 1/3, as in the Russian scaling laws, at higher frequencies.
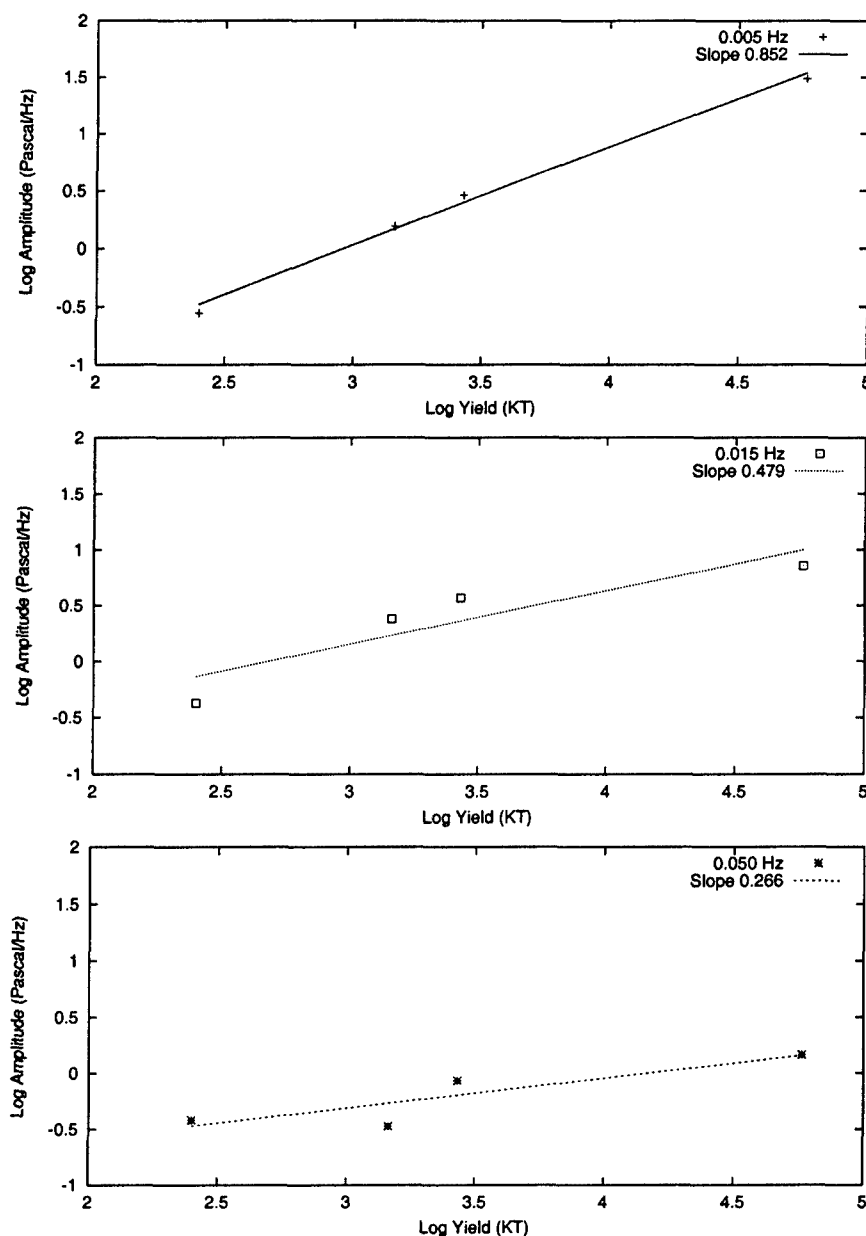
Figure 9. Spectral amplitude plotted vs. yield at frequencies of 0.005 Hz (top), 0.015 Hz (middle), and 0.050 Hz (bottom). The slope of the amplitude yield curve decreases with increasing frequency.

14
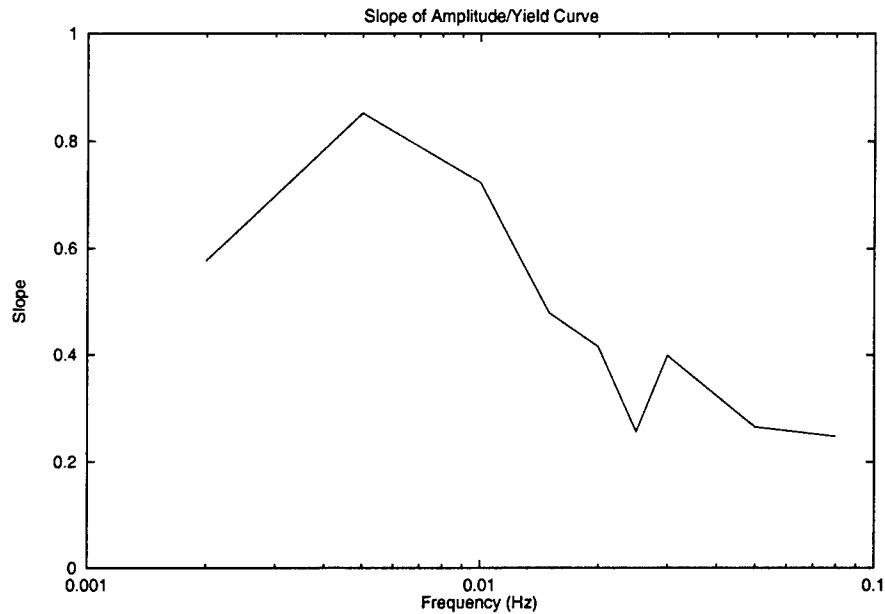
Figure 10. The slope of the log amplitude vs. log yield curve plotted as a function of frequency.

The strong dependence of the infrasound spectra on yield suggests that the explosion source function is much longer than the duration of the explosion and its associated near field nonlinear effects. As noted earlier, these effects last only a few seconds, while the spectral shape is affected at periods of hundreds of seconds.

2.6 Network Detection Simulations.

In order to predict the performance of the proposed 60 station IMS infrasound network, we modified the network simulation program NetSim (Sereno et al., 1990) to include the models of infrasound propagation described in Equations 11 and 12. NetSim uses these equations to calculate the pressures as a function of yield and range. These are used together with station locations, a noise model, a minimum signal to noise ratio for reliable measurement, and the number of stations required for a signal to be reported, to determine the network detection threshold as a function of position on the earth. We have calculated detection thresholds for the proposed IMS network using station dependent noise level estimates. The calculations were performed using the following parameters:

1. We used noise estimates from Blandford, et al (1995), which are based on wind measurements. The log noise levels (Figure 11) varied from −1.37 to −0.09 (Pascals), with the highest levels being in oceanic regions. Log standard deviation was taken to be 0.37.

2. Simulations were performed for two minimum signal to noise ratio levels: 2.0 and 1.5.

3. Two stations detect infrasound signals at a 90% confidence level.

4. Four element infrasound arrays increase signal to noise ratio by a factor of 2.

5. Propagation error has a log standard deviation in log signal of 0.3.

6. Station reliability is 95%.

15
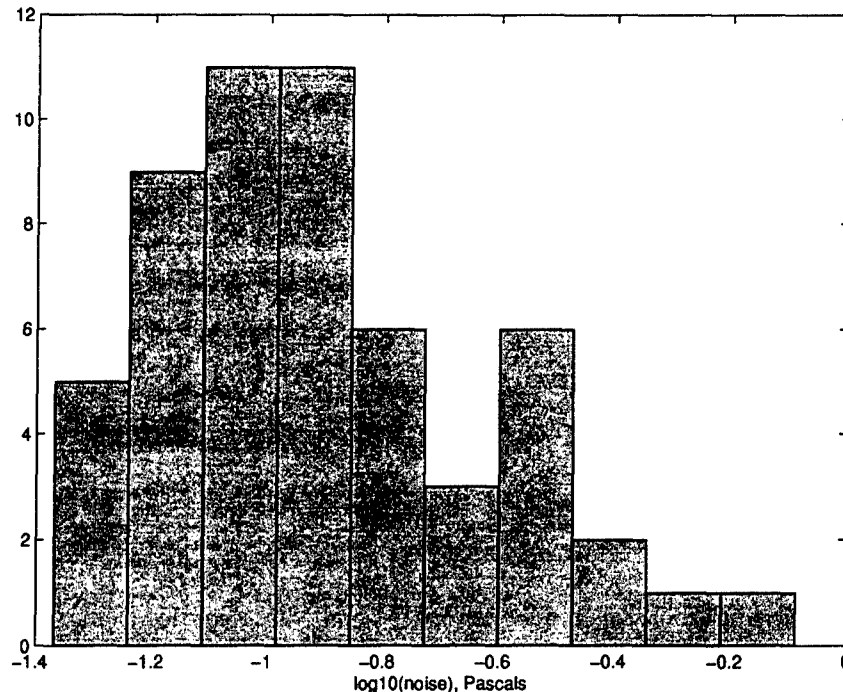
Figure 11. Frequency distribution of noise for the IMS network estimated from wind measurements by Blandford et al. (1995). Vertical axis is the number of stations in each 0.1 log amplitude bin. Horizontal axis is log noise amplitude in Pascals.

Detection threshold maps were calculated for the AFTAC and LANL scaling relations. The results are shown in Figures 12 to 15. Figures 12 and 13 were calculated with a minimum S/N of 2.0, and Figures 14 and 15 with a minimum S/N of 1.5. For the LANL model (Figures 12 and 14), the detection threshold is between 0.3 and 2 KT. For the AFTAC model (Figures 13 and 15), the detection threshold ranges from about 0.2 KT to about 1 KT. These scaling relations predict, therefore, that the infrasound detection threshold for the IMS network is less than the design goal of one kiloton in most locations, but higher in some regions, particularly in broad ocean areas.

The network simulation results indicate that the detection threshold of the future IMS infrasound network may be somewhat higher than the one-kiloton design goal in some locations. This result depends, of course, on a number of assumptions that went into the simulations. We made the assumptions that a four element array leads to a factor of two improvement in signal/noise ratio, that the noise levels at all stations are independent, and that a signal will be identified with a signal to noise ratio of 1.5-2. In general, these assumptions are optimistic, although experienced analysts may be able to detect a signal at lower S/N ratios. Improvements could also be made in the signal and noise modeling. Two improvements in particular which would make the simulations more realistic are:

1. including stratospheric winds, which would have the effect of improving detection in some directions and degrading it in others.

2. including actual noise distributions at each station instead of an average with a Gaussian distribution.

16
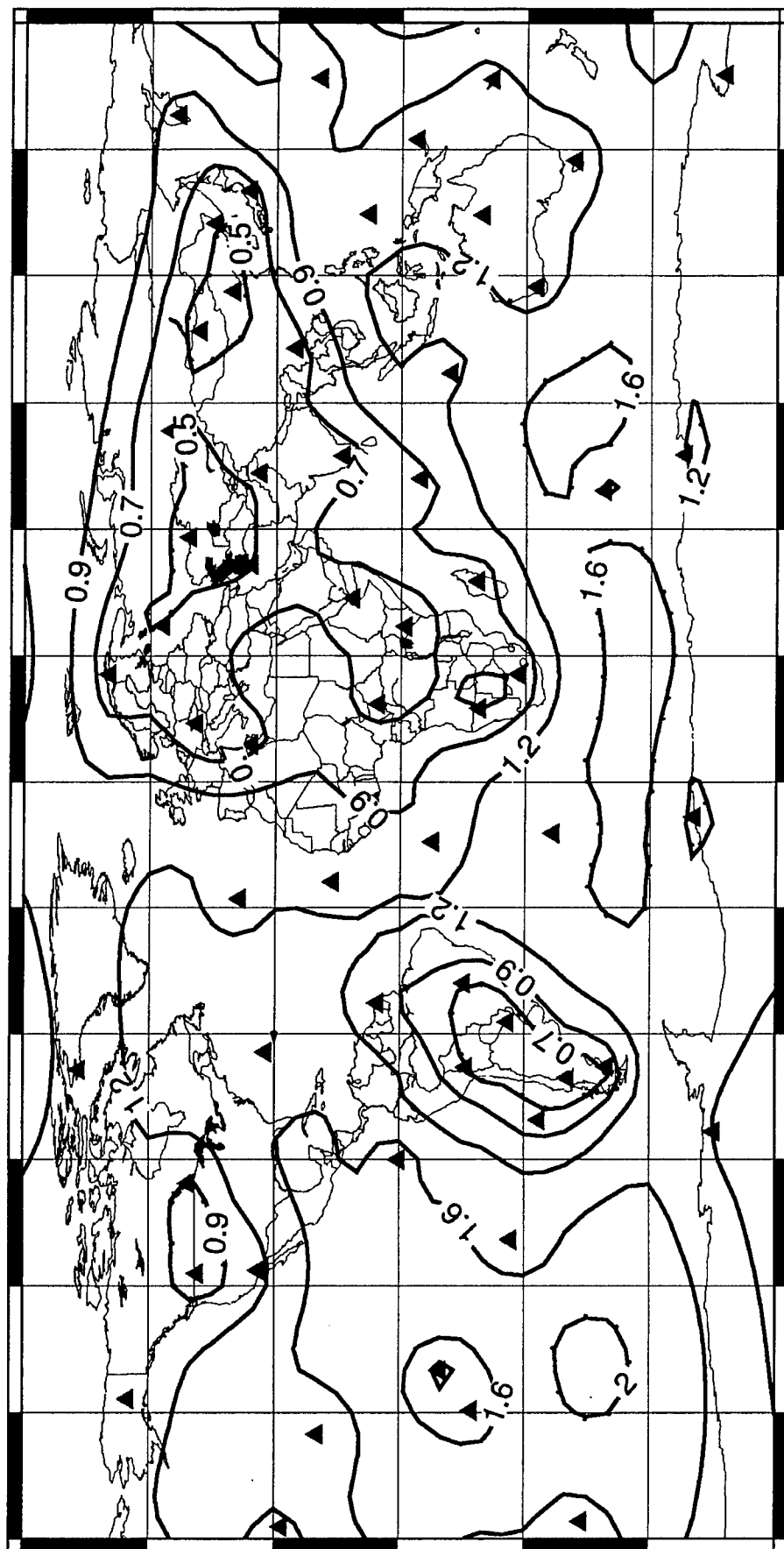
Figure 12. Contours showing detection thresholds with a 90% level of confidence for detection at 2 infrasound stations with station dependent noise levels using the LANL scaling relation (Equation 2). The intervals are logarithmically spaced with labels in kilotons. Minimum S/N is 2.

17
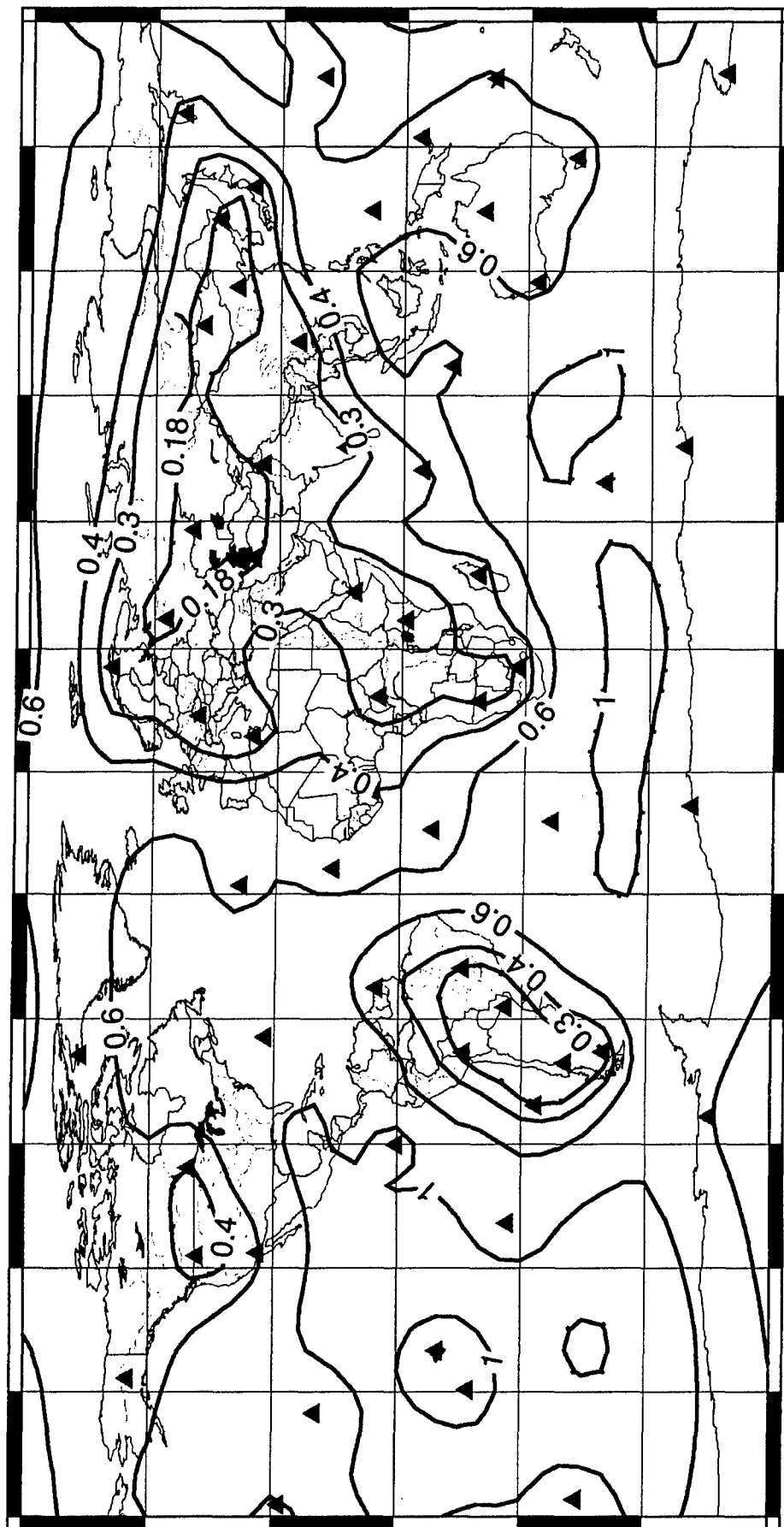
Figure 13. Contours showing detection thresholds with a 90% level of confidence for detection at 2 infrasound stations with station dependent noise levels using the AFTAC scaling relation (Equation 1). The intervals are logarithmically spaced with labels in kilotons. Minimum S/N is 2.
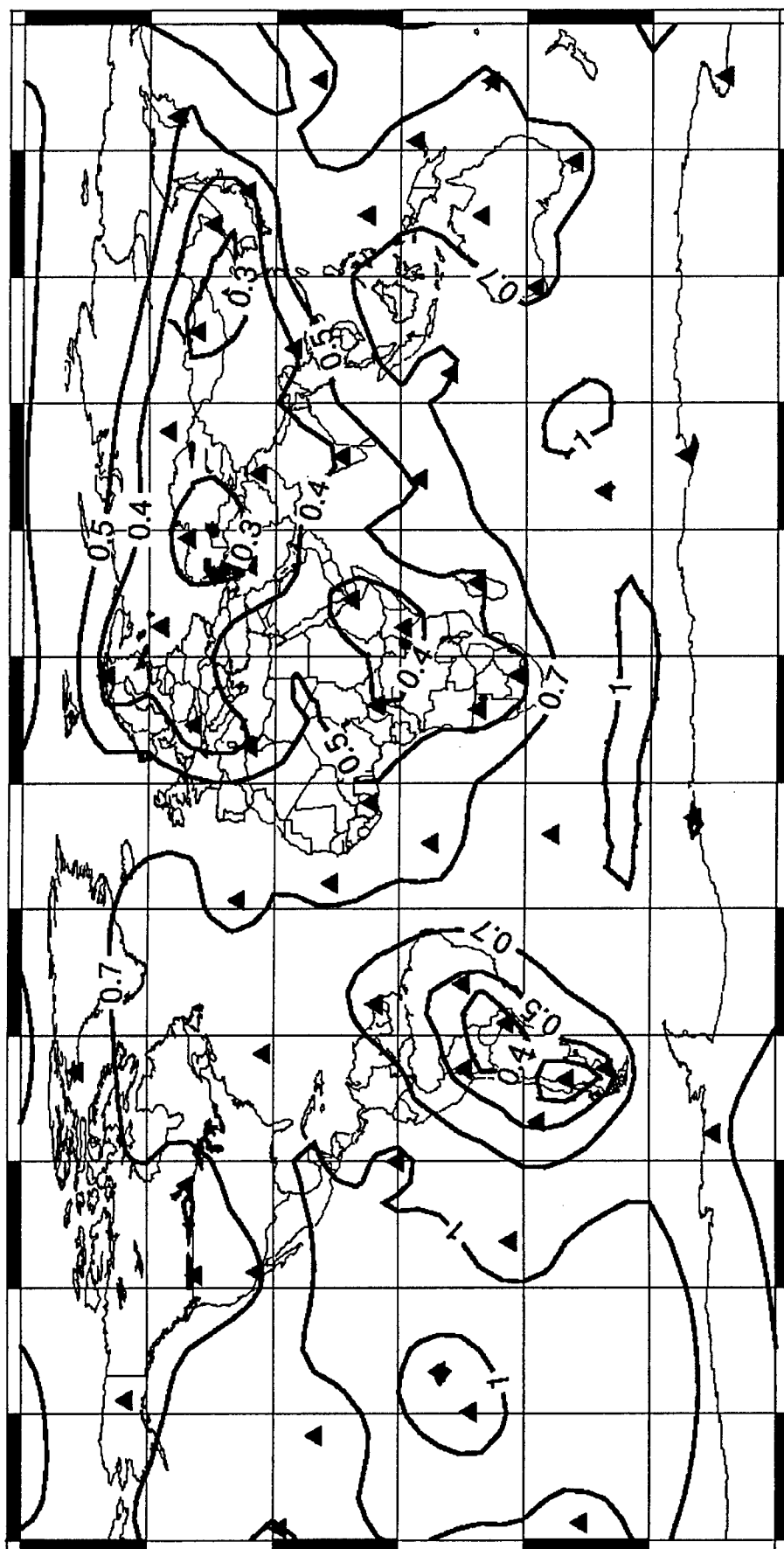
Figure 14. Contours showing detection thresholds with a 90% level of confidence for detection at 2 infrasound stations with station dependent noise levels using the LANL scaling relation (Equation 2). The intervals are logarithmically spaced with labels in kilotons. Minimum S/N is 1.5.
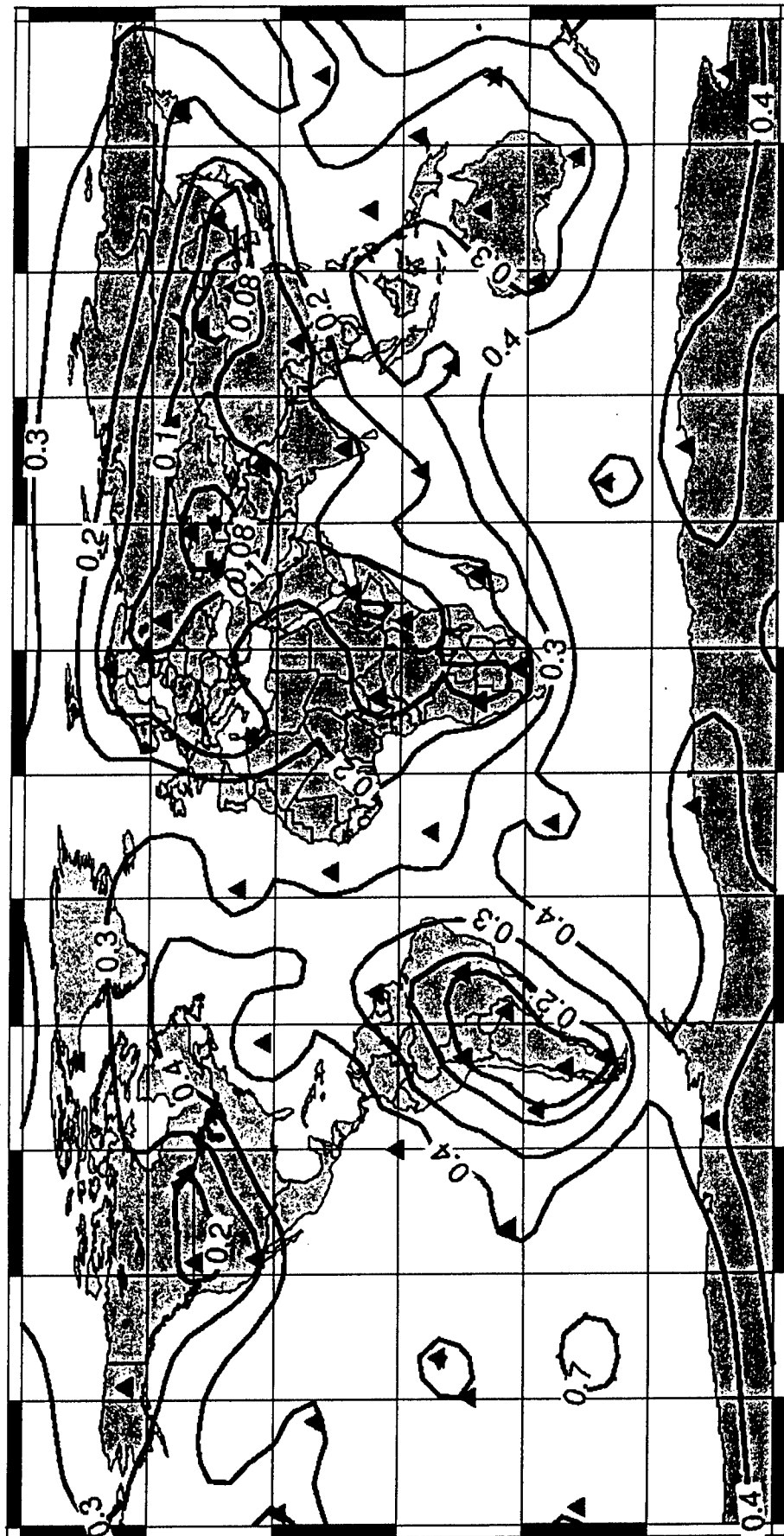
Figure 15. Contours showing detection thresholds with a 90% level of confidence for detection at 2 infrasound stations with station dependent noise levels using the AFTAC scaling relation (Equation 2). The intervals are logarithmically spaced with labels in kilotons. Minimum S/N is 1.5.

Figure 16, for example, shows the measured noise levels at the Los Alamos infrasound station as a function of time over a seven month period starting January 1999 as a time series and as a frequency distribution. Two features are apparent. First, the noise levels are time dependent, with higher noise levels in winter than in summer. Second, the noise distribution is skewed, and much higher than average noise levels are common.
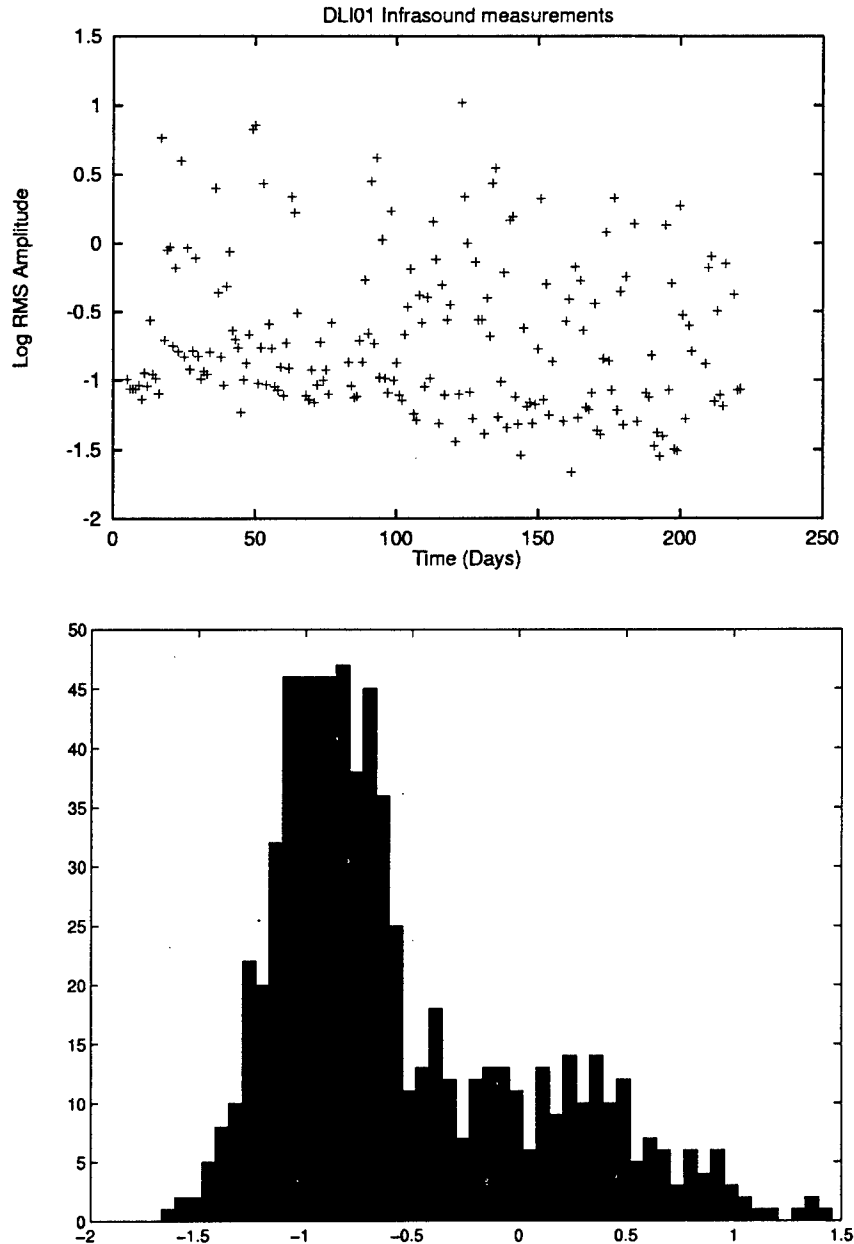
Figure 16. Noise measurements at the Los Alamos infrasound station for 7 month period starting January, 1999. The top figure shows the logarithm of the RMS noise amplitude taken at noon each day since the beginning of 1999. The bottom figure shows the frequency distribution of the noise measurements. The distribution of noise is both skewed and time dependent.
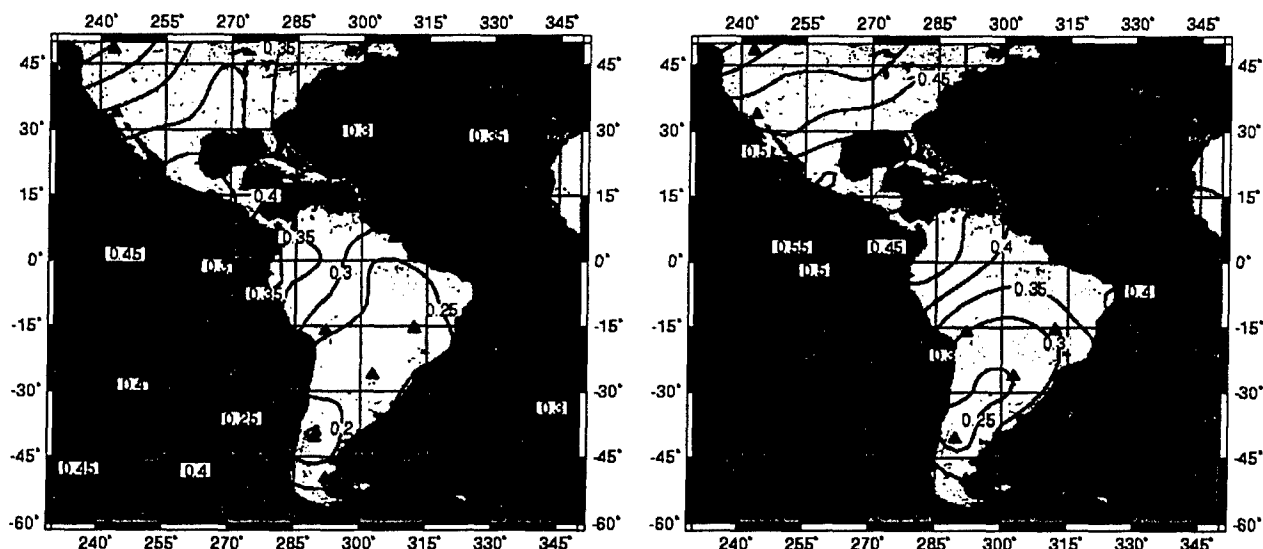
Figure 17. Threshold contours of yield in kilotons for 90% detection at 2 or more stations for the Gaussian noise model (left) and for the non-Gaussian noise model (right). Simulations were performed with XNICE.

NetSim does not have the capability to model non-Gaussian distributions, but they can be modeled with XNICE (Barker, 1996; Barker et al, 1994) (XNICE stands for the X Window version of the Network Identification Capability Estimation system, which can model network identification as well as detection capability). We modified XNICE to handle infrasound as well as seismic data, and did a test case to assess the difference caused by a realistic noise distribution such as that shown in Figure 16. We used a constant mean noise level at all stations of 0.1 Pascals and a minimum S/N of 1.5, and performed two test cases: one with a Gaussian distribution with a standard deviation of 0.64 (derived from the distribution in Figure 16), and one with the noise distribution modified to have the same shape as the distribution in Figure 16 at all stations. Figure 17 shows the results for South America. The effect of including the actual noise distribution is to increase the threshold level by about 50%, which is a significant difference. The IMS thresholds should be reevaluated as actual noise data becomes available for the IMS infrasound stations.

22

Section 3
Simulations of Pipe Array Amplitude and Phase Response and S/N Improvement

3.1 Introduction.

Pipes arranged in various configurations, leading to a pressure sensor, are used as spatial filters to enhance atmospheric infrasound signals relative to ground level pressure perturbations advected by the wind. We present a fast, accurate, computationally straightforward means of calculating pipe configuration responses, used with appropriate noise models, to facilitate the design of pipe array configurations for optimal signal-to-noise (S/N) improvement.

The numerical method is based on acoustic propagation in a tube, with computations utilizing propagator matrices. Experiments verify our assumption regarding the physical basis for the modeling and provide empirical measures of dispersion and attenuation. We estimate the amplitude and phase responses of two different types of pipes: open-ended pipes and closed-ended pipes with acoustic inlets along their lengths, and consider their relative merits. We then estimate response curves for a variety of pipe configurations, made of both pipe types.

Temporal and spatial distributions of pressure at the ground are complicated and difficult to predict, but are the major factor in signal-to-noise improvement for any pipe configuration. We use a self-similar noise distribution, as pressure variations at the frequencies of interest primarily result from a cascade of energy from larger to smaller eddies. Taylor's frozen turbulence hypothesis allows us to produce noise time series for each pipe inlet from the spatial noise model. We present the theoretically achievable signal-to-noise improvements, under different noise conditions, for pipe configurations spanning a range of shapes and sizes.

This paper is arranged into four distinct segments. In the first, we describe experiments designed to test assumptions regarding the physical basis for the modeling and to provide empirical measures of dispersion and attenuation. In the second, we describe the propagator matrix method we use for numerical simulations of any configuration. We next discuss the noise model used. Temporal and spatial distributions of pressure at the ground are complicated and difficult to predict. We consider the impact on S/N improvement for pipe configurations, of assumptions made regarding the noise model and of deviations from those assumptions. Finally, we present the results of simulations of amplitude and phase response curves for two types of pipes and of arrays of such pipes, and of S/N improvement for the arrays under a range of noise conditions, from which we draw conclusions regarding array design and areas for future work.

3.2 Background.

3.2.1 *The Basic Problem.*

Infrasonic signals of interest for monitoring nuclear explosions and for many natural phenomena (e.g. volcanic eruptions, bolides, aurora, sonic booms, and microbaroms; e.g. Wilson et al, 1996) generally have long wavelengths, 75 meters to 35 km, propagate at acoustic velocities and arrive at steep incidence, but overlap in frequency with pressure fluctuations due to turbulent eddies

near the ground which travel at the mean wind speed (e.g. Daniels, 1959). Arrays of pipes with acoustic inlets that span a large area and connect to a central manifold where the pressure is measured are used to filter out the spatially incoherent pressure fluctuations near the ground and so enhance the amplitude of steeply incident, long wavelength signals relative to the noise (e.g. Daniels, 1959; Burridge, 1971; Grover, 1971). This technique is effective, but not yet thoroughly quantified.

3.2.2. *Previous Work: Early Pipe Arrays.*

Much of the research on pipe arrays for infrasound instruments was performed prior to the 1963 Limited Test Ban Treaty, which banned nuclear explosions in the atmosphere, outer space, and under water. Daniels (1959) described the use of pipe arrays to improve S/N, where the noise is due to short wavelength atmospheric pressure fluctuations convected by wind. He used a tapered linear pipe with inlets along its length; their acoustic resistance matched to that of the local pipe dimensions to prevent extraneous reflections of signal within the pipe. Burridge (1971) and Grover (1971) addressed the design and performance of such arrays. Burridge presented a mathematical model of the response of a linear pipe, and demonstrated that non-tapered pipe would perform as well as tapered. He also considered the performance of a circular pipe with inlets. Grover (1971) reported on the actual performance of linear and circular pipes with acoustic inlets. Both noted that instruments should span sufficient area that noise coherence is minimized, but not so much that the phase is incoherent between signals received at different inlets. Other design considerations they present include the importance of choosing inlets acoustic resistances so that they balance the contribution of nearer and more distant inlets, and choosing the acoustic impedance of the pipe for a desired frequency response.

3.3 The Physical Basis for Modeling a Pipe Array Response.

Our goal is to build on the work described above to determine the response of pipe arrays and to develop design criteria for optimizing the S/N improvement. The first step is to determine the physical basis for modeling signal propagation within a pipe. The physical model used by Burridge (1971) was that of Benade (1968), for acoustic wave propagation in a cylindrical conduit. An alternate model however exists. For low Reynold's number incompressible fluid flow in a cylindrical conduit, resistance to flow is by viscous drag with zero velocity along the boundary. This causes laminar flow with a parabolic velocity gradient increasing radially inward, and is called Poiseuille flow. Grover (1971) demonstrated that the acoustic resistances of inlet ports were well approximated by Poiseuille flow, and Poiseuille flow was assumed to describe the attenuation in simulations of the response and noise reducing capabilities of permeable hose by McLaughlin, et al., 1997.

We have performed several experiments to determine how the infrasound signal propagates within hoses or pipes. The data collected also allow us to empirically determine parameter values for use in simulations.

3.3.1 *Velocity and Dispersion are Consistent with Acoustic Wave Propagation in a Cylinder.*

To assess the validity and accuracy of both the pressure gradient driven flow and acoustic wave models, we measure the velocity using two 10-meter lengths of 1.6 cm diameter permeable hose cut from the same 50 meter length (Figure 18). The hoses were parallel, within a couple centimeters of each other, and each was capped at one end and connected at the other end to identical, calibrated pressure transducers. A 30-meter section of 1.6 cm diameter impermeable hose was placed between one of the hoses and the transducer, allowing us to measure the velocity and dispersion due to propagation through impermeable hose independent of any effects of permeability.
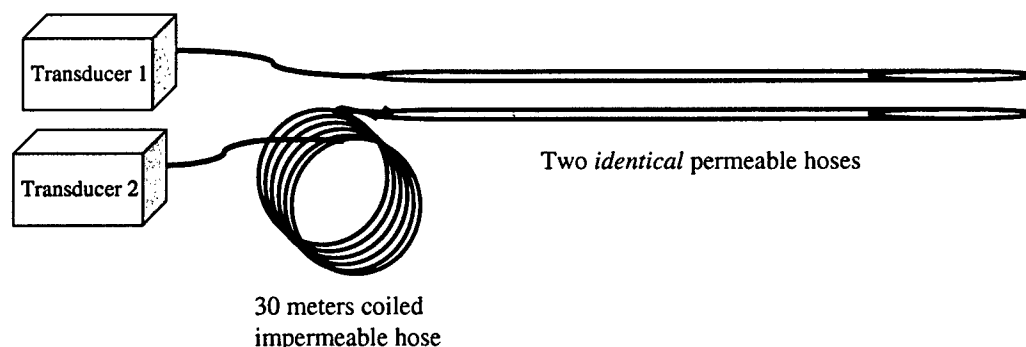
Figure 18. Layout of experiments described in text.

We induced pressure changes within a narrow, sealed, 11 meter long room and measured them with the apparatus shown in Figure 18, to provide input signals between 0.1 and 10 Hz, with amplitudes from 0.05 to 1 Pascal. Thus, these tests provide a measure of the hose response to signals in the frequency and amplitude range of interest for infrasound monitoring.

Signals from the two 10 meter permeable hoses, without the extra length of impermeable hose shown in Figure 18, correlate very well with zero time lag between them (Figure 19). When the extra 30 meters of impermeable hose is included, the signals also correlate well, but with a significant frequency-dependent time lag (Figure 19). The velocities indicate that the infrasound signals propagate as acoustic waves in the hoses, not as pressure gradient driven flow. Unfortunately, significant deviations in signal amplitude between supposedly *identical* 10 m permeable hoses (for the experimental setup without the 30 m impermeable hose) preclude measurement of attenuation as a function of frequency. We experimented with a few different segments of hose cut from a single originally 50 m long hose. The differences are presumably due to variations in leak rate between the hoses. Such variability is important to document as it necessitates the use of other materials when the instrument response must be precisely known.

The dispersion is greater than predicted, with group velocities measured by cross-correlation approaching 150 m/s near 0.1 Hz. Predictions are based on the linear transmission line formalism used to describe the acoustical properties of a tube (Benade, 1968; Haak and de Wilde, 1998).

The greater than predicted dispersion may have the same cause as the greater than predicted attenuation, discussed next, as the theoretically dispersion and attenuation are related through the propagation constant of the hose.
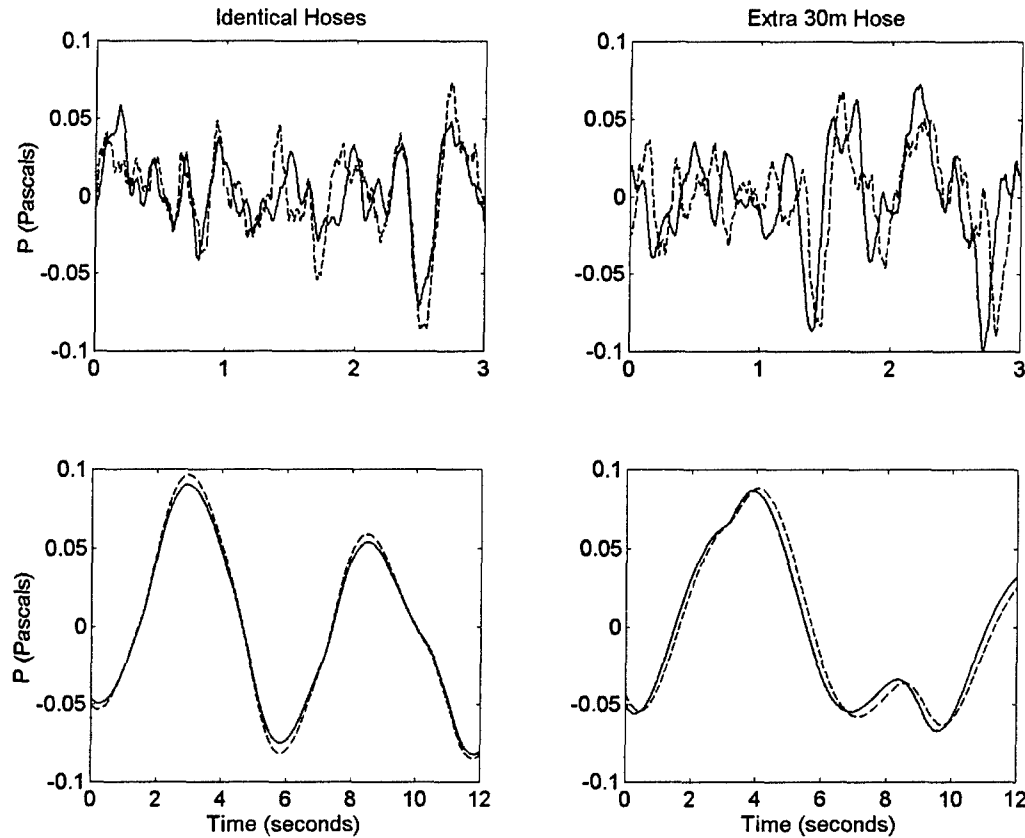
Figure 19. Segments of signals recorded by the apparatus shown in Figure 18, filtered from 1-5 Hz (top) and from 0.05 - 0.2 Hz (bottom). Those in the left column were recorded with no extra hose, and the maximum cross-correlation of each is at zero lag. Those on the right had a 30 m impermeable hose interspersed between the end of one permeable hose and the transducer (dotted line). In that case, the maximum cross-correlations are at 0.080 (top) and 0.122 seconds lag (bottom), indicating significant dispersion of the signal.

3.3.2 *Measured Attenuation is much Greater than Predicted.*

The loss mechanisms for Poiseuille flow and acoustic waves in a cylinder are similar, in that they both lose energy in the viscous boundary layer along the cylinder wall. Further, for frequencies of interest, infrasound wavelengths are greater than the longest pipes being considered. Thus, all the air in the hose may effectively be moved as a unit due to the pressure pulse applied at one end and so attenuation would result from drag within the boundary layer between the wall and the mass of air, similar to the attenuation for pressure gradient driven flow. Finally, we note that the formulas for acoustic propagation based on transmission line theory are for an infinitely long tube. As we discuss below, a steady state boundary layer may not develop for acoustic waves in the length and radii tubes considered here. Thus, although the velocity and dispersion measurements demonstrate that the signal propagates as an acoustic wave, if the boundary layer

26

is laminar, the attenuation predicted for Poiseuille flow could be more appropriate for these long wavelength signals.

We measured attenuation directly by recording pressure signals before and after propagation along 30, 40, and 60 m lengths of impermeable hose, using the setup illustrated in Figure 21. As with the velocity and dispersion measurements, these results provide insight into the controlling physical processes as well as permitting empirical determination of parameter values for use in modeling.
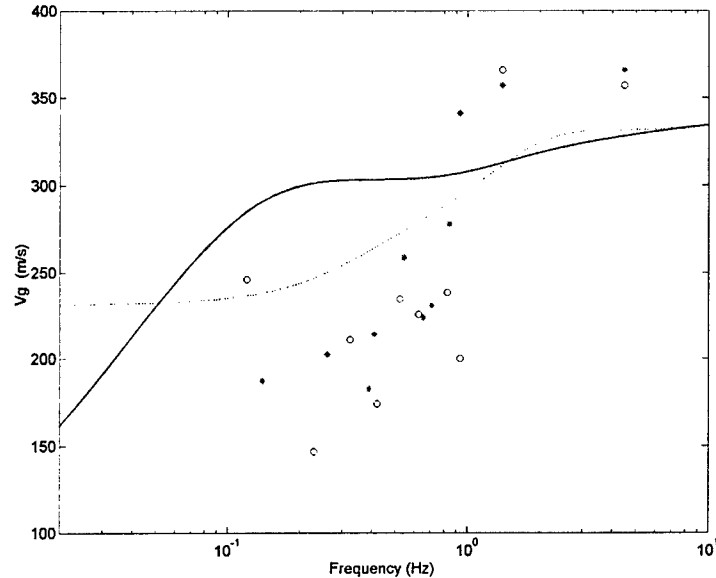
Figure 20. Theoretical group velocity curves for acoustic waves in cylindrical conduits (Benade, 1968; Haak and de Wilde, 1998), and group velocity measurements from experiments such as illustrated in Figure 18. The solid and dashed curves are, respectively, group velocities for acoustic waves in a cylinder for the viscosity of air and for a 7 times higher viscosity term, to account for possible non-laminar resistance to shear and inertial terms. The two symbols represent dispersion measurements from two distinct repetitions of the experiments.
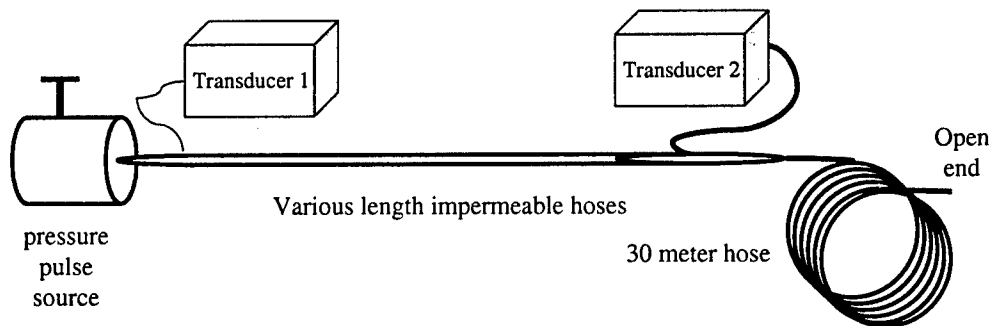
Figure 21. Layout of experiments to measure attenuation. We used this setup with 30, 40, and 60 meter lengths of impermeable hose. The extra 30 m length of hose at the end ensured that reflections from the end did not affect the results.

27

The signal frequency typically peaked around 2-4 Hz in these experiments. Figure 22 shows the observed values and the predicted attenuation for 3 Hz acoustic waves, using two values for viscosity, for various length hoses.
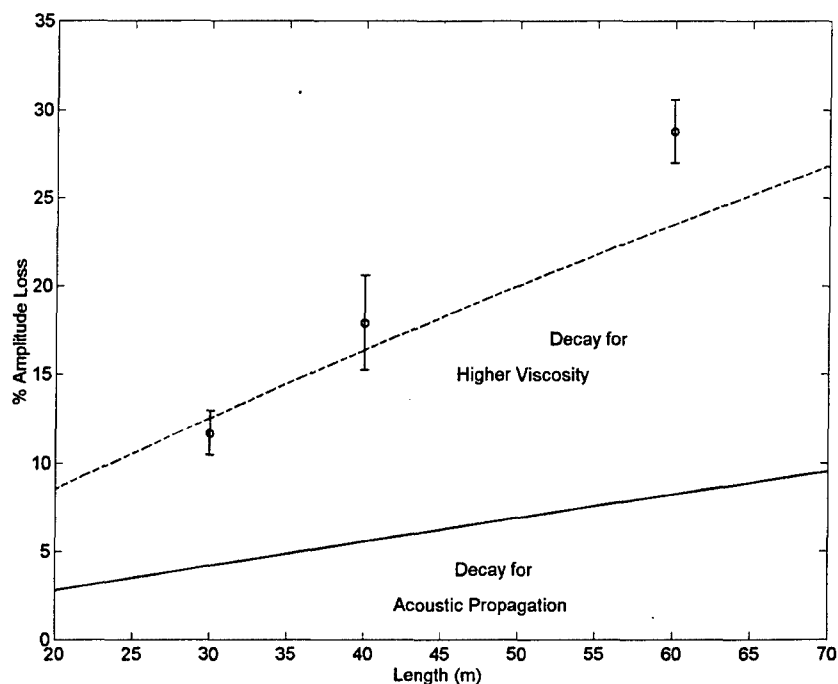
Figure 22. Predicted and observed signal decay as a function of length of the hoses. The solid line indicates the decay predicted for acoustic waves in 1.6 cm diameter hoses for 3 Hz waves. The dashed line indicates the decay predicted using a larger viscosity value empirically determined to better fit the data. The error bars indicate 2 standard deviation uncertainty bounds for observed attenuation for 30, 40, and 60 meter long hoses.

Neither attenuation nor dispersion is modeled accurately by the equations for acoustic propagation in a cylinder. Therefore, for numerical simulations we use an empirically determined measure of viscosity that improves the data fit (Figures 20 and 22).

These results are consistent with those of Stevens et al. (1998), in which the decay of Helmholtz oscillations within tubes was much greater than predicted for viscous shear in a laminar boundary layer. They also found that the attenuation is independent of whether a hose is permeable or impermeable. That is, the amplitude loss due to leakage through inlets, or permeable hose, was separable from that due to propagation losses, and the propagation losses were independent of the conduit permeability. The importance of this is that air movement through inlets does not interfere with propagation through the pipes, so the same attenuation constant can be used in simulations of either type of hoses, or for pipes with or without inlets.

3.3.3 Functional Dependence of Dispersion and Attenuation on the Propagation Constant.

Attenuation is proportional to $e^{re(\Gamma)}$, while phase velocity is given by $V_p = \omega/\text{Im}(\Gamma)$, where Γ is the propagation constant discussed in the following section. While we use the exact expressions for Γ in our calculations, the much simpler long period, small tube approximation for Γ is appropriate for much of the frequency band of interest and is more illuminating for this discussion. In that approximation, Γ approaches

$$\Gamma \rightarrow \left(\frac{\omega}{c}\right)\left\{\left(\frac{2\gamma}{3}\right)^{1/2}\left[1+\left(\frac{6}{r_v^2}\right)^2\right]^{1/4}\right\}(1-i),\qquad(17)$$

where ω is angular frequency, c is sound velocity in air, γ is the ratio of specific heats at constant pressure and volume C_p/C_v, and r_v is the ratio of the cylinder radius to the viscous boundary layer thickness (Benade, 1968; Haak and de Wilde, 1998). That ratio is given by

$$r_v = \left(\frac{\omega\rho}{\eta}\right)^{1/2}a,\qquad(18)$$

where ρ and η are the density and viscosity of air, and a is the cylinder radius (Benade, 1968).

While useful models, even the complicated *exact* expression for Γ relies on assumptions that are violated in practice. We discuss two. First, the expressions are for infinitely long tubes, and so do not take into account that steady state may not be reached in the short pipes considered here. Thus, the equations lack inertial terms describing the acceleration of air in the pipes by an acoustic wave. Second, roughness in the pipe interior is ignored. Such roughness could effectively increase the thickness of the boundary layer. We cannot at this time resolve the true physics behind the observed dispersion and attenuation. These considerations however provide reason for replacing the viscosity term with a larger, empirically determined value. The empirical term could represent the additional resistance due to inertia, greater boundary layer thickness, or flow that is not laminar either because steady state is not reached or because the wall roughness causes turbulence. We note that the eddy viscosity, used to describe viscous-like effects in turbulent flow, can easily be 1 to 2 orders of magnitude greater than the fluid viscosity (e.g. Schlichting, 1960). Since Γ increases with viscosity, an increase in the effective viscosity increases both the attenuation and dispersion. This is illustrated in Figures 20 and 22, where dashed lines show that both the predicted group velocity and amplitude loss are better fit when we incorporate an empirical viscosity term 7 times greater than that of the viscosity of air.

3.3.4 Summary and Conclusions Regarding Physical Model.

Acoustic wave propagation in a cylinder is consistent with experimental measurements of velocity. Attenuation and dispersion however are much greater than predicted. We therefore base our simulations on the equations for acoustic propagation, with the viscosity term replaced by an empirically determined value that provides numerical results that better match observations.

Different materials used to construct spatial filters might produce quite different attenuation, due for example to differences in interior surface roughness. Thus, we recommend that attenuation be

determined empirically for whatever materials are used. The theoretical attenuation for Poiseuille flow is a likely minimum value for the real attenuation.

3.4 Numerical Simulation Method.

3.4.1 *The Propagator Method for Sound Transmission in a Pipe.*

As developed and detailed by Burridge (1971), a propagator method can be used to model acoustic propagation within a pipe, due to pressure fluctuations at inlets. For a harmonic pressure fluctuation, $p(x)e^{i\omega t}$ and a harmonic volume flux $f(x)e^{i\omega t}$ at a distance x from the left end of a pipe (Figure 23), the resulting flux-pressure vector $\begin{pmatrix} f \\ p \end{pmatrix}$ propagates through an impermeable section of length l according to

$$\begin{pmatrix} f(x+l) \\ p(x+l) \end{pmatrix} = \begin{pmatrix} \cosh\Gamma l & -\dfrac{1}{Z_0}\sinh\Gamma l \\ -Z_0\sinh\Gamma l & \cosh\Gamma l \end{pmatrix}\begin{pmatrix} f(x) \\ p(x) \end{pmatrix} = M\begin{pmatrix} f(x) \\ p(x) \end{pmatrix}, \tag{19}$$

(Burridge, 1971). Γ and Z_0 are the propagation constant and characteristic impedance of the pipe. We generally use here the expressions of Haak and de Wilde (1998), which are equivalent formulations to those of Benade (1968). In that formulation, $\Gamma = \sqrt{ZY}$, and $Z_0 = \sqrt{Z/Y}$, where $Z = i(\omega\rho/\pi a^2)(1-F_v e^{i\phi_v})^{-1}$ and $Y = i(\omega\pi a^2/\rho c^2)(1+(\gamma-1)F_t e^{i\phi_t})$, ω is angular frequency, ρ is density, a is pipe radius, c is the acoustic velocity in air, and γ is the ratio of specific heats at constant pressure and volume. $F_v e^{i\phi_v} = \dfrac{2J_1(r_v\sqrt{-i})}{r_v\sqrt{-i}J_0(r_v\sqrt{-i})}$ and $F_t e^{i\phi_t} = \dfrac{2J_1(r_t\sqrt{-i})}{r_t\sqrt{-i}J_0(r_t\sqrt{-i})}$, where J are complex Bessel functions, r_v is as defined in equation 2, and $r_t = a(\omega\rho C_p/\kappa)^{1/2}$ is the ratio of the pipe radius to the thermal boundary layer thickness, where C_p is the specific heat of air at constant pressure, and κ is the thermal conductivity.

For an inlet at x, the resulting flux-pressure vector propagates from one side of the inlet (x_-) to the other side of x (x_+) according to

$$\begin{pmatrix} f(x_+) \\ p(x_+) \end{pmatrix} = \begin{pmatrix} 1 & -\dfrac{1}{Z_k} \\ 0 & 1 \end{pmatrix}\begin{pmatrix} f(x_-) \\ p(x_-) \end{pmatrix} + \begin{pmatrix} Pe_k/Z_k \\ 0 \end{pmatrix} = N\begin{pmatrix} f(x_-) \\ p(x_-) \end{pmatrix} + \begin{pmatrix} Pe_k/Z_k \\ 0 \end{pmatrix}, \tag{20}$$

where Pe is the pressure disturbance at the inlet and Z_k is the impedance of the inlet. Therefore, the flux-pressure vectors at two points along a pipe, x_1 and x_2 (Figure 23), are related by the propagator matrices representing the inlets and distances between inlets as follows,

$$\begin{pmatrix} f(x_1) \\ p(x_1) \end{pmatrix} = M_{Nb+1}\prod_{i=Nb}^{1}N_iM_i\begin{pmatrix} f(x_2) \\ p(x_2) \end{pmatrix} + M_{Nb+1}\left[\begin{pmatrix} Pe_{Nb}/Z_{Nb} \\ 0 \end{pmatrix} + \sum_{j=2}^{Nb}\prod_{i=Nb}^{j}N_iM_i\begin{pmatrix} Pe_{j-1}/Z_{j-1} \\ 0 \end{pmatrix}\right] \tag{21}$$

$$= A\begin{pmatrix} f(x_1) \\ p(x_1) \end{pmatrix} + B$$

where Nb is the number of inlets between x_1 and x_2. The inlets are numbered as 1, 2, ..., Nb between x_1 and x_2. The N's are the propagator matrices at the inlets, defined in equation (4), M's are propagator matrices between inlets, and M_1, M_{Nb+1} are the propagator matrices between x_1 and the first inlet and between x_2 and the last inlet. A and B are therefore the complete propagator matrices from x_1 to x_2. We next apply this method to derive the response of the pipe arrays.
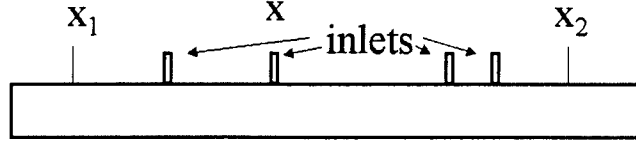
Figure 23. Pipe configuration.

3.4.2 Formulas for Pressure at the Center of Close-Ended Pipe Arrays.

For a set of pipes arrayed radially and connected to a summing manifold at the center (Figure 24, upper left and center), using the above method, the pressure response at the center is

$$
p = \frac{\sum_{i=1}^{R} \left[\frac{A_{12}^{(i)}}{A_{22}^{(i)}} B_2^{(i)} - B_1^{(i)} \right]}{\sum_{i=1}^{R} \frac{A_{12}^{(i)}}{A_{22}^{(i)}}}, \tag{22}
$$

where R is the total number of radial pipes and the A's and B's are the propagator matrices from the pipe ends to the center for each pipe, as defined in (19).

For a hexagonal system as shown in Figure 24 (upper right), the pressure response at the center is

$$
p = \frac{\sum_{i=1}^{R} \left[\frac{S_1^{(i)}}{S_2^{(i)}} T_2^{(i)} - T_1^{(i)} \right]}{\sum_{i=1}^{R} \frac{S_1^{(i)}}{S_2^{(i)}}},
$$

$$
\begin{pmatrix} S_1^{(i)} \\ S_2^{(i)} \end{pmatrix} = A^{(i)} \begin{pmatrix} X^{(i)} \\ 1 \end{pmatrix}, \begin{pmatrix} T_1^{(i)} \\ T_2^{(i)} \end{pmatrix} = A^{(i)} \begin{pmatrix} Y^{(i)} \\ 0 \end{pmatrix}, \tag{23}
$$

$$
X^{(i)} = \frac{{}^{(l)}A_{12}^{(i)}}{{}^{(l)}A_{22}^{(i)}} + \frac{{}^{(r)}A_{12}^{(i)}}{{}^{(r)}A_{22}^{(i)}}
$$

$$
Y^{(i)} = -\frac{{}^{(l)}A_{12}^{(i)}}{{}^{(l)}A_{22}^{(i)}} {}^{(l)}B_2^{(i)} - \frac{{}^{(r)}A_{12}^{(i)}}{{}^{(r)}A_{22}^{(i)}} {}^{(r)}B_2^{(i)} + {}^{(l)}B_1^{(i)} + {}^{(r)}B_1^{(i)}
$$

where $A^{(i)}$ is the propagator matrix from the pipe end to the center for the ith radial impermeable pipe, $^{(l)}A^{(i)}$, $^{(l)}B^{(i)}$ and $^{(r)}A^{(i)}$, $^{(r)}B^{(i}$ are, respectively, the propagator matrices from the left and right ends to the center of each transverse pipe joined to the radial pipe i, The right subscripts denote components of matrices.

Equations (22) and (23) provide the responses of two different pipe arrays. These are straightforward to construct for any number of radial and transverse pipes, and for irregular combinations of pipes with unevenly distributed angles and different radii. The responses at the center are represented as the sum of all the pipe contributions. The method is directly applicable as well to configurations of open-ended pipes, such as those in the lower row of Figure 24.
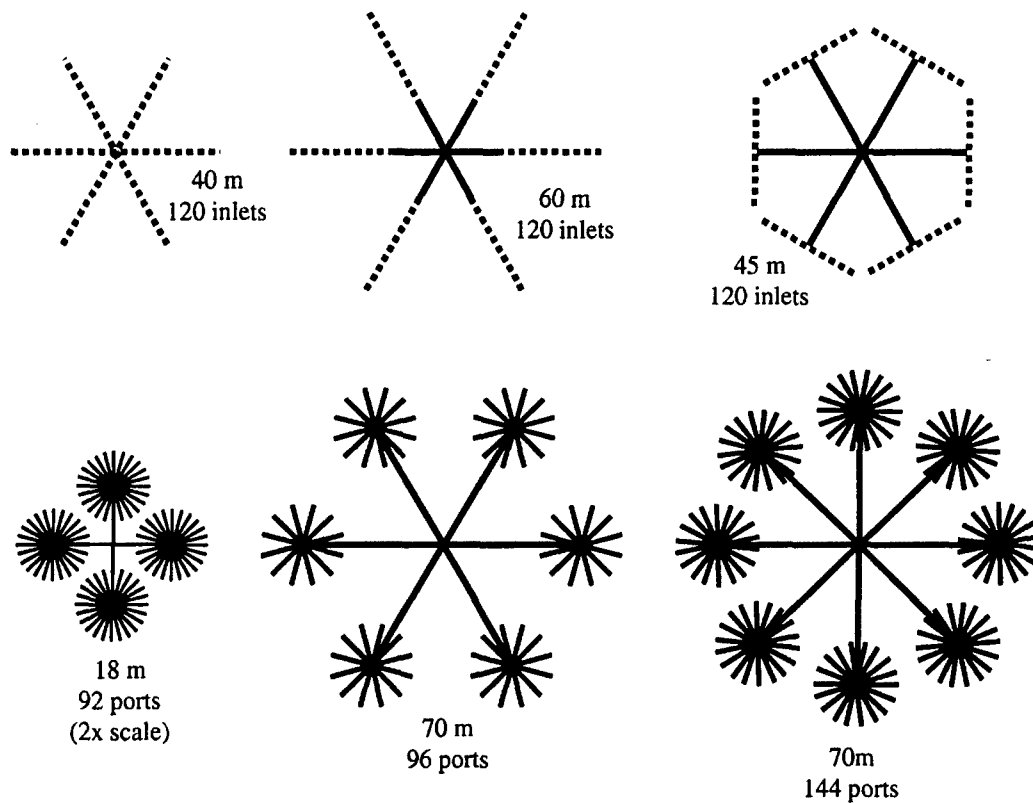
Figure 24. Designs for which we simulate S/N enhancement. Those along the top row are constructed of 2.5 cm radius pipes with 100 acoustic ohm inlets every meter (dotted lines) connected to impermeable pipe (solid lines). Pressure is measured at a summing manifold at the center of each configuration. Designs along the bottom row consist of sets of essentially open-ended impermeable pipes arranged radially (in practice a screen mesh may cover the ends, but this is acoustically insignificant). The long radial arms are 0.95 cm radius, and the shorter arms (and all pipes in the 18 m diameter configuration) are 0.64 cm radius. Summing manifolds are at the center of each set of radial arms, which are then connected by the long radial pipes to a central summing manifold where the pressure is measured.

32

3.5 Noise Models.

3.5.1 *Noise Model Used.*

The performance of a pipe array depends on the character of the noise, and so meaningful modeling of infrasound pipe array performance hinges on accurate knowledge of the temporal and spatial distribution of pressure fluctuations over the array. We discuss the physical basis for the noise model chosen and limitations imposed by necessary simplifications.

Pressure variations across the ground are assumed to be due to and linearly related to turbulent eddies, which are generally represented as perturbations to the mean wind velocity (e.g. Stull, 1988; Kaimal and Finnigan, 1994). The scale of eddies depends on the boundary layer thickness, and within a canopy, depends on the canopy height. Large turbulent eddies are generated by buoyancy driven convection, typically due to heating of the surface layer over land. Smaller eddies are then generated, as wind shear in the boundary layer breaks up the large eddies. Eddies in the scale length of interest for infrasound are in the inertial subrange of the turbulent kinetic energy (TKE) spectrum. That is, they are due to a cascade of energy from larger to smaller eddies. We use a zeroth order Von Karmann, or self-similar, distribution to represent that distribution. That is defined by a correlation function of $K_0(r/a)$, where K_0 is the zeroth order Bessel function (e.g. Frankel and Clayton, 1986).

Taylor's frozen turbulence hypothesis is almost universally assumed in studies of wind near the ground surface (e.g. Kaimal and Finnigan, 1994; Stull, 1988). It assumes that eddies evolve slowly compared with the time it takes for the mean wind velocity to transport them past a point on the ground and that all sizes of eddies move at the same (wind) velocity. The assumption is ubiquitous because it permits the transformation of a time series measured at one point to an estimate of the spatial dimensions of eddies. Taylor's hypothesis holds to first order in many situations, and we assume it for our simulations, which allows us to transform the simulated, self-similar, spatial pressure variations into time series at each instrument port.

3.5.2 *Complexities in Real Noise: Impact on Results and Areas for Further Research.*

A Von Karmann noise model represents a simplification of the real physics. Turbulence in the atmospheric boundary layer, and particularly near the ground and in canopies is very complex. We consider briefly the potentially most important deviations from the simple model we assume, since complexities not incorporated into the noise model may effect the accuracy of simulations of array performance.

Stull (1988) reports that Taylor's hypothesis generally holds when the turbulent intensity, given by the standard deviation of wind speed, is much less than the mean wind speed. In practice, this means it breaks down under very gusty conditions. Evolution of eddies over time periods less than it takes for them to pass over a point should lead to less spatial coherence, and so better performance. Since such conditions tend to exist at higher wind velocities, we might expect performance to deteriorate less than linearly with the amplitude increase that comes with a mean wind speed increase (e.g. McDonald, et al., 1971).

Kaimal and Finnigan (1994) note that larger eddies tend to travel more rapidly than smaller ones, especially in plant canopies. Taylor's hypothesis assumes that all eddies move at the same speed. The impact of eddy size and wind speed is not entirely intuitive. It is obvious that a large eddy covering a significant portion of the array will contribute to shorter period noise the more rapidly it moves. Small eddies however, can also lead to surprisingly significant noise coherence, and so little S/N improvement, as the same signal traverses subsets of inlets at some time lag. The size and velocity together, of the eddies, will determine which frequencies are affected. If accurate measures of such features of the noise distribution are available for a site, they could be incorporated into simulations to indicate how the S/N will be affected.

The TKE spectrum may be spiked at wavenumbers corresponding to particular obstructions to the wind. In a canopy, tree trunks, brush, or grasses may break down larger eddies into eddies too small to be at all coherent between inlets. Thus, denser canopies with more small-scale structures near the ground should provide advantages over more open canopies. In the case of larger, topographic obstructions, Kaimal (1998) reports that a "hill wake may be detectable many tens of hill lengths downwind." This is an important consideration in siting.

Another feature of wind in canopies that may be important for pipe array design is the existence of horizontal and vertical gusts on the scale of the canopy height. This produces a non-trivial third moment, or skewness, in the TKE spectrum (e.g. Kaimal and Finnigan, 1994; Finnigan and Brunet, 1995). A vertical gust that spans a single pipe configuration could be indistinguishable from an infrasonic signal at that single receiver.

Finally, we note that the scale of spatial coherence of wind can be many times greater parallel to the mean wind velocity, than normal to it (McDonald et al, 1971; Finnigan and Brunet, 1995). For sites where the wind comes from a single predominant direction for the vast majority of the time, better performance may be achievable with fewer inlets using an asymmetric array that takes advantage of the asymmetry of the wind coherence. Where instrument siting options are limited, simulations that include such complications in the noise model will provide more reliable predictions of performance.

Because S/N improvement depends on decorrelation over time at a single inlet, and spatially over multiple inlets, the unmodeled complexities of the noise described above will affect the accuracy of the S/N improvement simulation. Thus, the discussion above should provide direction for future work with the goal of enabling better modeling of the noise structure, including better understanding its genesis. The first step in that effort should be to better quantify the spatial statistics of pressure variations, to provide real spatial and temporal noise models with correlations accurately determined for different types of sites. In addition, current site surveys are performed with a single sensor, requiring Taylor's hypothesis for transformation to produce a spatial noise model. Consideration should be given to performing future site surveys with an array of sensors, in order to capture rather than assume the spatial distribution of noise.

3.6 Simulations.

3.6.1 *Overview.*

We perform simulations for the 6 different configurations of pipe arrays shown in 24. Each of the basic configurations have been deployed by infrasound researchers or considered for deployment as part of the International Monitoring System (Christie, 1999). These configurations are of two distinct types. One type is made up of impermeable pipes and close-ended pipes with small inlets of high acoustic impedance along their lengths. These are similar to arrays constructed of permeable hose. The other type uses impermeable pipes with open ends, providing almost no acoustic impedance mismatch with the atmosphere. Both types of configurations use one or more summing manifolds where multiple pipes meet. We assume that the manifold volumes are minimal. If that straightforward engineering constraint is not met, reflections off the manifolds could lead to poorer performance.

3.6.2 *Amplitude and Phase Responses of Open and Closed End Pipes.*

The responses of open-ended pipes vs. closed-ended pipes with acoustic inlets differ in some important respects (Figures 25 to 29 We illustrate these differences by comparing the responses of two pipes, both 60 meters long. One is open-ended, but with no acoustic inlets. The second is closed-ended, with one acoustic inlet of 100 acoustic ohms resistance in the center. The amplitude response of the open pipe is flat up to the frequency where resonance occurs, while the closed-ended pipe acts like a low pass filter (Figure 25 The corner of the filter depends on the acoustic impedance of the inlets and the radius of the pipe.

Resonance interferes with high frequency signals. The first resonance peak for open-ended pipes occurs at a frequency of f=V_{a_a}/2L, where L is the pipe length and V_a is the acoustic wave speed. For closed-ended pipes there is an interference null at that frequency. Our highest frequency of interest determines how long of pipes we may use.
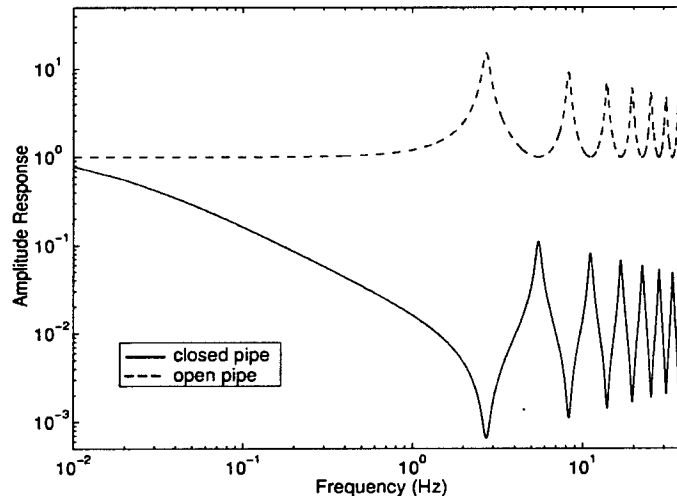
Figure 25. Amplitude response of a 60 m open-ended pipe (dashed) and a 60 m closed-ended pipe with a 100 acoustic ohm inlet at its center (solid), both with a radius of 1.25 cm.

35

For a constant inlet impedance, the amplitude response of the closed-ended pipe also varies with radius (Figure 26). The wider the pipe is, the smaller the amplitude response is. For a wide pipe, the impedance is small compared to that of the inlet, and so the pressure perturbation that can be achieved within the pipe is small. A physically intuitive explanation for this is that only a small pressure perturbation is permitted by the small inlet, and the larger the volume of the pipe, the more that signal is diluted. This is not a problem for open-ended pipes.
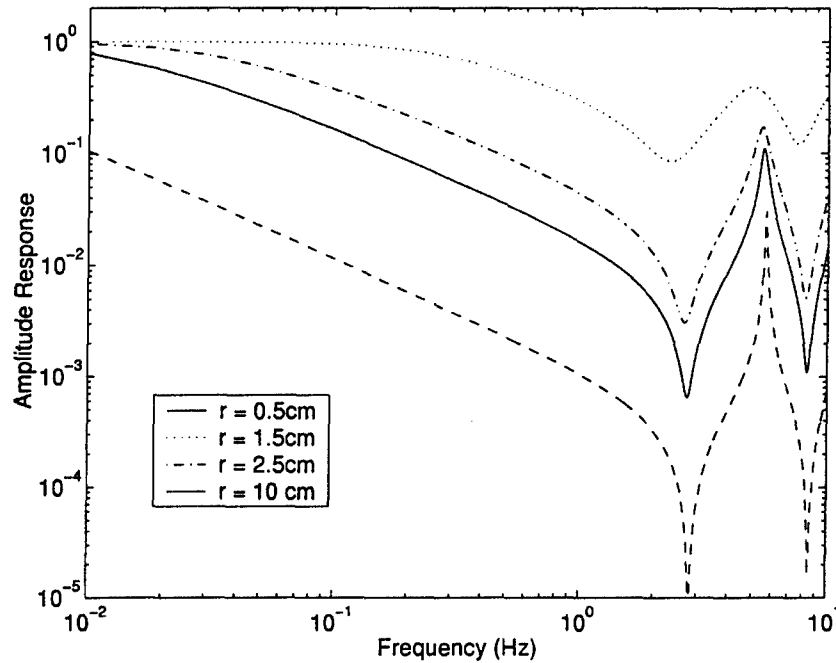
Figure 26. Amplitude response of 60 m long closed-ended pipes of four different radii, each with a single 100 acoustic ohm inlet in the pipe center. The first resonance peaks are slightly shifted because the acoustic velocity is less in the narrower pipe.

The phase response is nearly constant for the widest close-ended pipe because the impedance of the pipe is quite small for all frequencies of interest, relative to that of the inlet (Figure 27). The impedance, however, increases for narrower pipes and lower frequencies. For sufficiently narrow pipes and low frequency, the pipe impedance is similar to that of the inlet and so there is less delay. Because there is still a mismatch between the inlets and the narrow pipe response at higher frequencies, there is a large change in phase delay from low to high frequency. Our calculations assume a constant impedance inlet, an approximation valid as long as the impedance of the inlet is much less than that of the pipe. Thus, the approach of the phase response curves to zero really represents an upper bound on the rate at which they will asymptotically approach zero delay. The important points demonstrated here are the trade-offs between pipe radius, inlet impedance, and amplitude and phase response. There is also a trade-off between pipe radius and the useful frequency band near the first resonance peak. That is, at the high frequency end of the curves, the phase response changes abruptly at the resonance peak. The curve of the narrowest (lowest impedance) pipe is much smoother. Thus, the same resonance peak affects a wider frequency range in a narrower pipe.
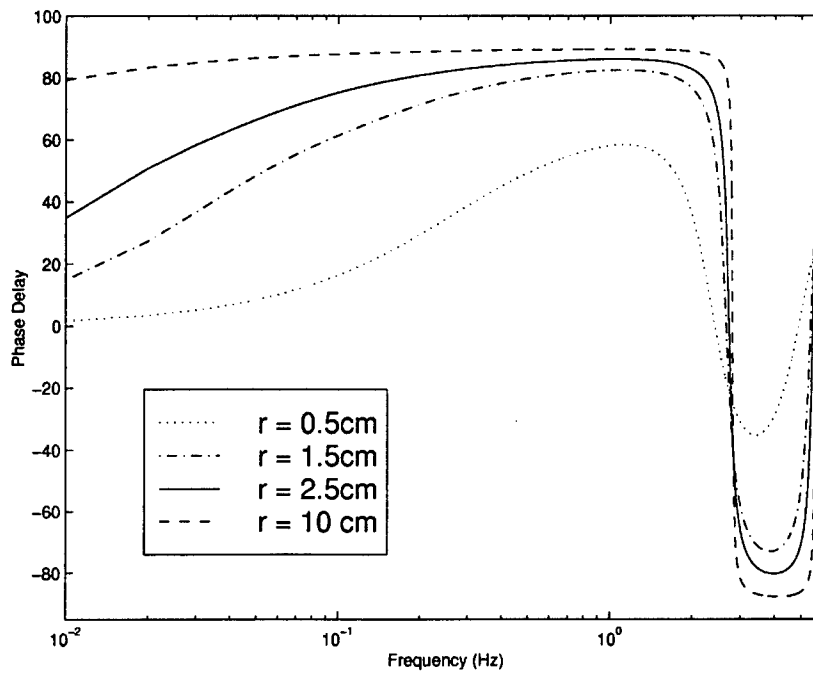
Figure 27. Phase response of four 60 m long closed-ended pipes of different radii, each with a 100 acoustic ohm inlet at their centers.

The amplitude (Figure 28) and phase (Figure 29) responses of the open-ended pipes are quite flat up to the resonance peaks.
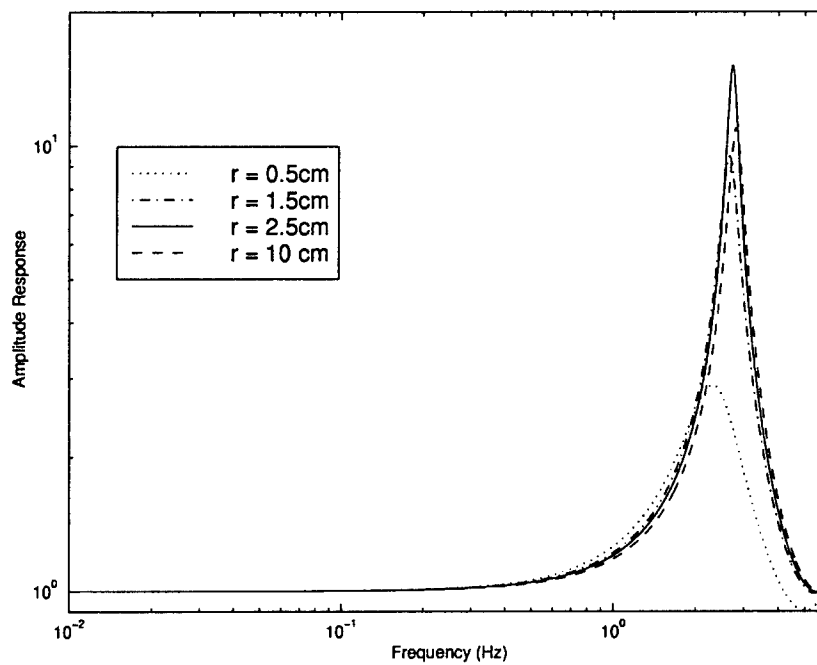
Figure 28. Amplitude responses of 60 m open-ended pipes of various radii.
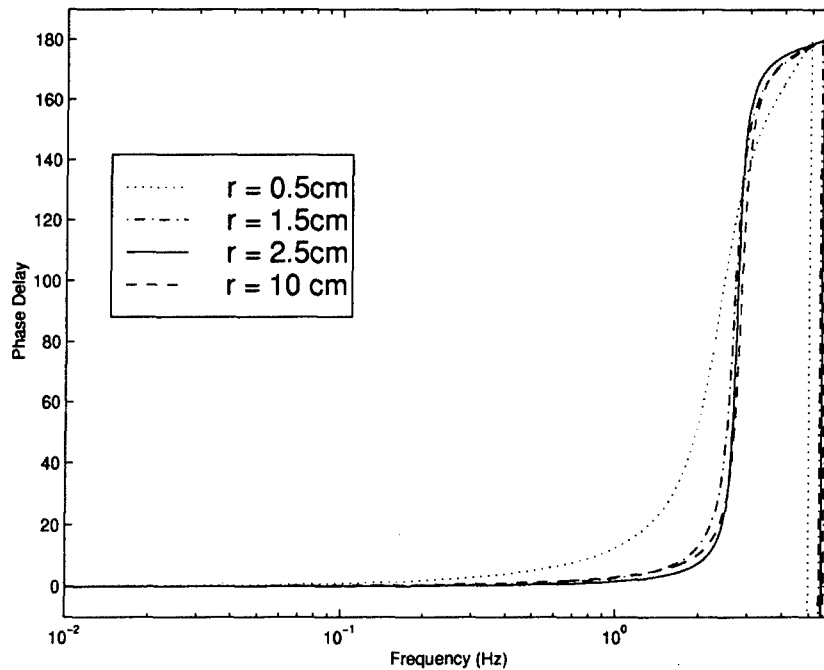
Figure 29. Phase responses of 60 m open-ended pipes of various radii.

Open-ended pipes appear to have the advantage over closed-ended pipes with small acoustic inlets, as they provide flat phase and amplitude responses, although the addition of multiple inlets does flatten the amplitude response of the close-ended designs somewhat. Infrasound spatial filters made of pipes with inlets or permeable hoses are commonly used and have a long history, although the advantages of open-ended pipes have begun to be recognized (e.g. Christie, 1999). We simulate the performance of configurations with both types of pipes in the next section.

3.6.3 *Pipe Array Configurations.*

Three closed-ended configurations modeled include the common radial arm design (e.g. Noel and Whitaker, 1991), a modified radial arm to prevent coherent noise near the center from dominating, and a hexagonal design (Christie, 1999) intended for more widely distributed spatial sampling (Figure 24). The open-ended designs are variations on one suggested by Alcoverro (1998), and include a small aperture design for low wind conditions, and two 70 m diameter configurations with 96 and 144 ports, intended for long -period recording under high wind conditions (Christie, 1999).

3.6.4 *Amplitude and Phase Responses of Different Configurations.*

Figure 30 shows the amplitude responses of the configurations shown in Figure 24. The configurations using closed-ended pipes (hexagonal and two radial configurations, light lines) all act as lowpass filters, while the open-ended pipe configurations have flat amplitude responses up to the resonance frequencies.

38
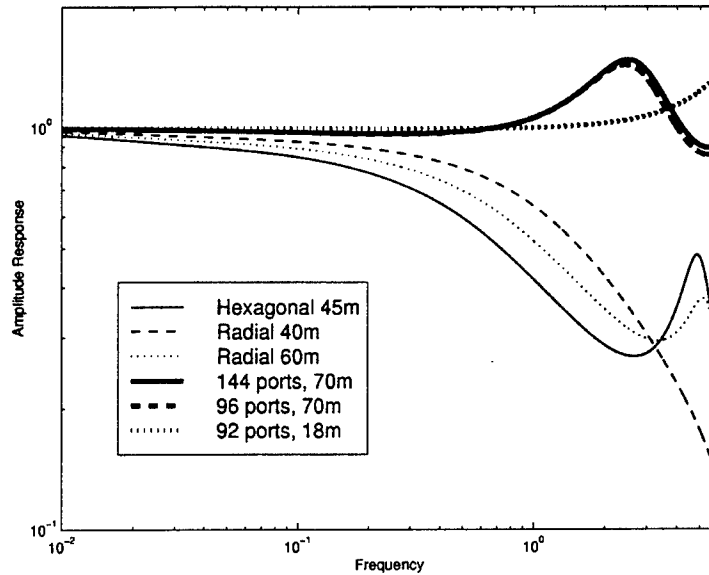
Figure 30. Amplitude response of the configurations shown in Figure 24.

The phase response of the open-ended pipes is flat up to the resonance frequency. The influence of the resonance frequency however extends quite a ways. The extent of that influence could be minimized without badly effecting the amplitude response, by the use of slightly wider radius pipe (see Figure 27).

The closed-ended pipes have phase delays of approximately 50° at 1 Hz, well before the resonance frequency has any effect. The phase delay however is not as severe as that for a single inlet (Figure 27), since the impedance mismatch between the sum of the 120 inlets and the pipe is less than it is for a single inlet. These configurations consist of 2.5 cm radius pipes. Narrower pipes would reduce the phase delay further and provide an overall higher amplitude response for these closed-pipe configurations.
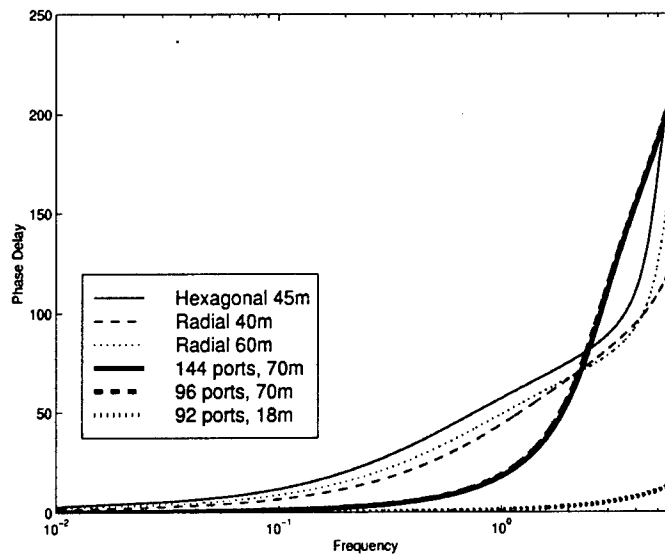
Figure 31. Phase response of the configurations shown in Figure 24.

39

3.6.5 *Signal to Noise Improvement.*

We compare the improvement in S/N ratio measured at the central manifold of each configuration shown in Figure 24 over that recorded with no pipe array. If the noise were spatially uncorrelated, the S/N improvement would simply be $\sqrt{n}$, where n is the number of ports or inlets. We use a vertically incident plane wave signal and Von Karmann distributed noise with correlation lengths of 1 and 10 meters (Figure 32). As discussed above, we assume that the noise field remains stable as it is carried passed the instrument. This feature of the noise has a tremendous impact on the performance of any instrument.

Both greater correlation lengths and lower wind speeds lead to lower frequency pressure variations at any single spatial position (Figure 33). This is due to the advection of stable correlated noise and will impact each instrument similarly.

Advection of spatially correlated noise leads to temporal correlations at individual ports or inlets. That is, pressure variations at two ports aligned along the wind direction will be highly correlated at a time lag of $\tau = D/V_w$, where D is the distance between ports, and V_w is the wind speed. At signal periods much greater than τ, the two ports have highly correlated inputs and will not contribute to increasing the S/N. Ports separated by less than the correlation length, in any direction, will also have highly correlated inputs at zero time lag. Thus, we see that smaller diameter configurations, longer correlation length noise, and higher wind speeds lead to poorer low frequency performance (Figure 34). In the extreme case of noise with a correlation length much greater than the array diameter, the noise would be coherent over much of a pipe array and would sum as coherently as steeply incident signals.

On the other hand, at frequencies of $f = V_w/2 \cdot D$, the signals will be negatively correlated at ports aligned with the wind direction and separated by a distance D, as defined above. This occurs in some of the simulations, where, at certain frequencies we observe a better than $\sqrt{n}$ improvement in S/N, where n is the number of ports (Figure 34). Even small deviations from our ideal noise model will make that less likely to occur in real noise conditions. The spectra shown are good guides to expected performance, but such fine details should not be over-interpreted.

We do not complicate the presentation of results by scaling the noise amplitude by the wind speed, although higher wind speeds are clearly associated with higher amplitude pressure variations (e.g. McDonald et al, 1971). Such complications could be simply factored into the results after calculations for unit signal and noise levels have been made, so comparison can be made of effective S/N ratios under different wind conditions.
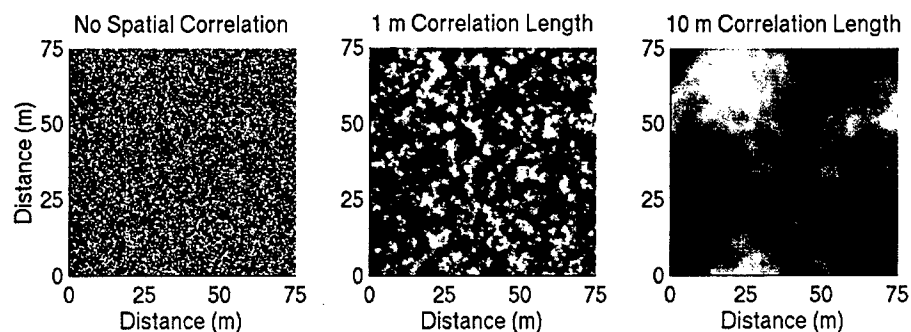
Figure 32. Seventy-five by seventy-five meter samples of spatially uncorrelated, and 1 and 10 meter correlation length, Von Karmann distributed noise.
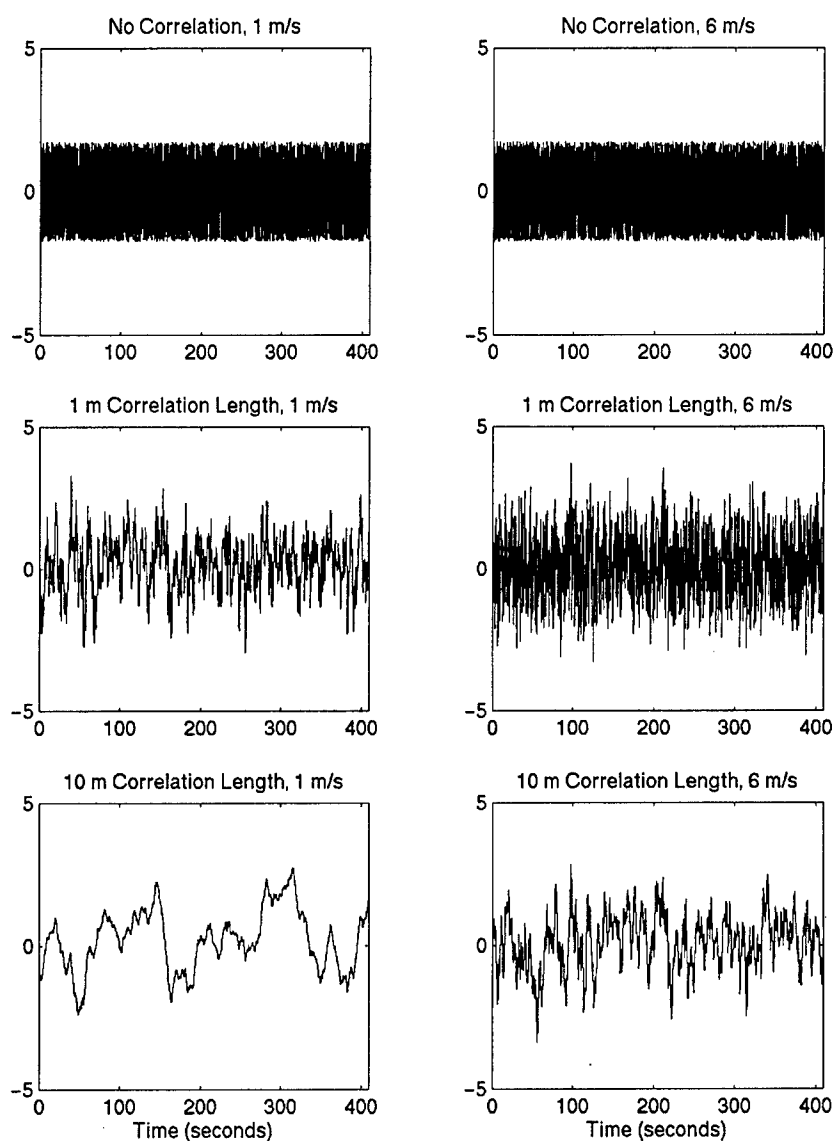
Figure 33. Pressure variation time series observed at a single point due to advection of the three different noise fields (Figure 32) at 1 m/s (left column) and at 6 m/s (right column).
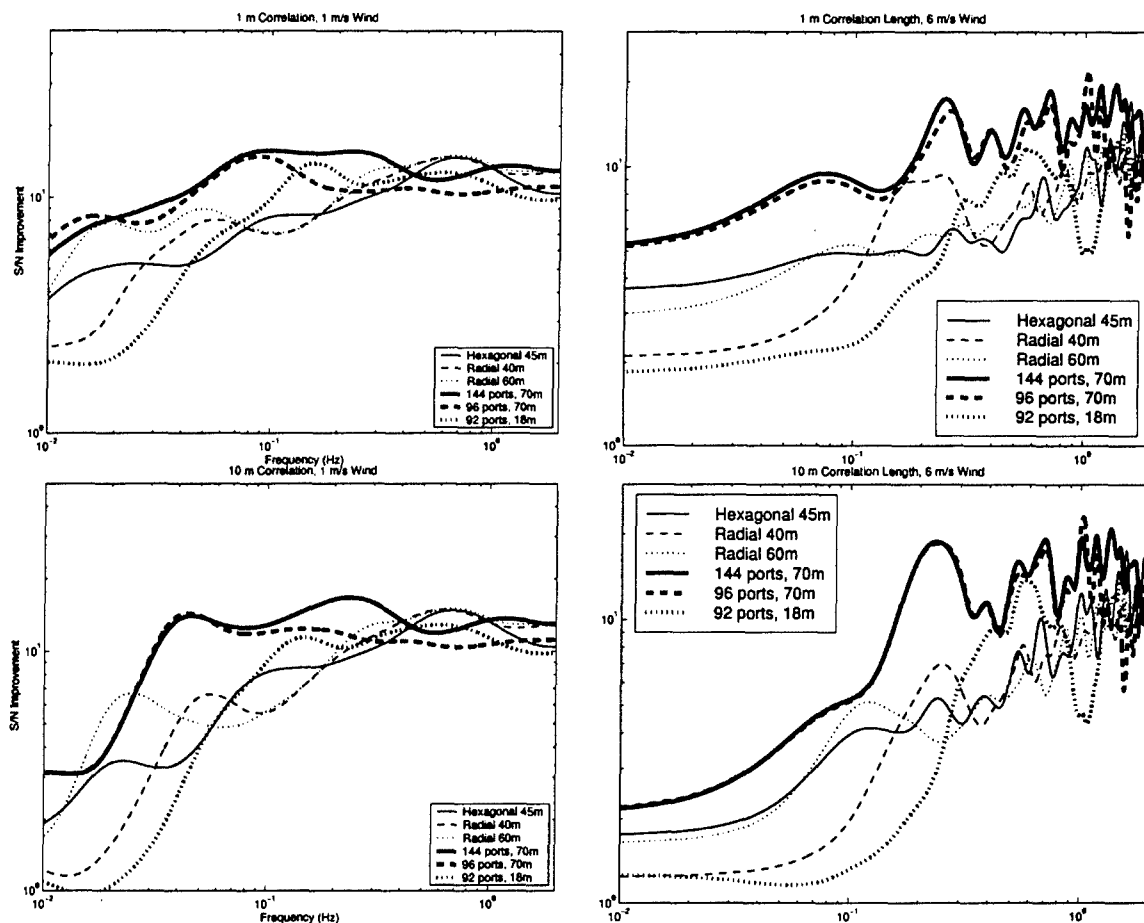
Figure 34. S/N improvement for six different configurations (Figure 24), for 1, and 10 m correlation length self-similar noise, carried past the instruments by 1 and 6 m/s winds. Maximum radius spanned and number of ports (for open-ended pipes) are listed. Each of the close-ended pipe configurations has 120 inlets. For uncorrelated noise, S/N improvement will simply be a constant $\sqrt{n}$ improvement, where n is the number of ports.

3.7 Conclusions

Acoustic propagation in a cylindrical conduit provides a good physical basis for modeling the response to an infrasound signal of an array of pipes. Actual attenuation and dispersion however can be much greater than predicted, indicating that the particular pipes used should be calibrated.

A self-similar noise distribution provides an appropriate and simple noise model, as pressure variations in the frequency of interest primarily result from a cascade of energy from larger to smaller eddies. Taylor's frozen turbulence hypothesis allows us to produce noise time series at each pipe inlet from the spatial noise model. Both assumptions together enable us to produce noise time series at each pipe inlet that have realistic relationships with the noise series at all the other inlets.

42

Open-ended pipes hold most of the advantages over closed-ended pipes with high impedance acoustic inlets. Specifically, the open-ended pipes have essentially flat amplitude responses, while the closed-ended pipes act as lowpass filters. The open-ended pipes also have flat phase responses, while the phase responses of the closed-ended pipes vary much more across the spectrum of interest. In general, the acoustic impedance of inlets and radii of closed-end pipes must be carefully matched to achieve a desired response curve, and even then, it will not be flat.

The advantages described above suggest that for most purposes, open-ended pipes will be preferable. For permanent installations, pipes are certainly preferable, but permeable hose has been a mainstay of temporary field campaigns for volcanic monitoring. Our results indicate that flatter amplitude and phase response functions could be obtained, while maintaining the low expense and simple transport and set-up of hoses, by switching from permeable to open-ended impermeable hoses.

The most important design criterion for enhancing S/N is having sufficient spatial sampling. Extra ports, however, provide no advantage if spaced more closely than the noise correlation length. All configurations performed well, and similarly, at high frequencies, as the high frequency noise has the least spatial correlation. The differences in performance are very significant at the lower frequencies. The two 70 m diameter configurations provide the best performance in our simulations of S/N enhancement, and their performances were nearly identical even though one had 144 ports and the other had only 96. The 18 m diameter configuration performed the worst at low frequency.

We have developed a rapid, accurate, method of estimating the performance of any pipe configuration used for infrasound recording. The method is based on acoustic propagation in a cylinder, the computations are based on propagator matrices, and results match experimental data. This tool will permit numerical simulation-based optimization of new designs before deployment, thus speeding up development and testing of new designs. It will also enable optimization of configurations where noise conditions are well known, and estimation of response curves for existing instruments. The most important step that can be taken now to improve instrument performance is to obtain, and utilize in such modeling, more complete and accurate noise models.

Section 4
Electronic Addendums

There are two electronic addendums to this report. They are:

1. The complete digitized data set of infrasound recordings; and

2. The final report from IDG which includes additional measurements derived from the data and discussion of azimuthal variations due to wind.

Section 5
References

Alcoverro, B. (1998), Acoustic filters design and experimental results, *Proceeding: Workshop on Infrasound*, Commissarriat à l'Énergie Atomique, Bruyères le Châtel, France. (Unclassified)

Barker, T.G. (1996), "Xnice: A System for Assessing Network Identification Performance," Maxwell Laboratories Scientific Report to Phillips Laboratory, PL-TR-96-2087. (Unclassified)

Barker, T. G., K. L. McLaughlin, and J. L. Stevens (1994), "Network Identification Capability Evaluation (NICE)", S-CUBED Technical Report to the Advanced Research Projects Agency SSS-TR-94-14701, July. (Unclassified)

Benade, A.H. (1968), On the propagation of sound waves in a cylindrical conduit, *J. Acoust. Soc. Am.*, **44**, 616-623. (Unclassified)

Blandford, R. R. and D. A. Clauter (1995), "Capability Estimation of Infrasound Networks", AFTAC report. (Unclassified)

Blandford, R. R., D. A. Clauter, R. W. Whitaker, and T. Armstrong (1995), "Infrasound Network Options," AFTAC/DOE White Paper. (Unclassified)

Brown, D. J. (1999) "Summary of Infrasound Source Location Meeting: San Diego, November 9-10, 1998, Center for Monitoring Research Technical Report CMR-99/02, January. (Unclassified)

Burridge, R. (1971), On the propagation of sound waves in a cylindrical conduit, *Geophys. J. R. Astr. Soc.*, **26**, 53-69. (Unclassified)

Christie, D.R. (1999), Wind-noise reducing pipe arrays, memo of the Provisional Technical Secretariat, CTBTO, Vienna, Austria. (Unclassified)

Clauter, D. A. and R. R. Blandford (1998), "Capability Modeling of the Proposed International Monitoring System 60-Station Infrasonic Network," proceedings of the Infrasound workshop for CTBT monitoring, Santa Fe, New Mexico, August 25-28, 1997, LANL report number LA-UR-98-56. (Unclassified)

Daniels, F.B. (1959), Noise reducing line microphone for frequencies below 1 c/s, *J. Acoust. Soc. Am.*, **31**, 529. (Unclassified)

Finnigan, J.J. and Y. Brunet (1995), Turbulent airflow in forests on flat and hilly terrain, In *Wind and Trees,* pp 3-40, M.P. Coutts and J.Grace (eds.), Cambridge University Press. (Unclassified)

Frankel, A. and R. Clayton (1986), Finite difference simulations of seismic scattering: Implications for the propagation of short-period seismic waves in the crust and models of crustal heterogeneity, *J. Geophys. Res.,* **91**, 6465-6489. (Unclassified)

Grover, F.H. (1971), Experimental noise reducers for an active microbarograph array, *Geophys. J. R. Astr. Soc.,* **26**, 41-52. (Unclassified)

Haak H.W. and G.J. de Wilde, On the propagation of low frequency sound waves in porous hoses used in infrasound detection systems, pre-print. (Unclassified)

Kaimal, J.C. and J.J. Finnigan (1994), Atmospheric Boundary Layer Flows: Their Structure and Measurement, Oxford Univ. Press. (Unclassified)

McDonald, J.A., E.J. Douze, and Eugene Herrin (1971), The structure of atmospheric turbulence and its application to the design of pipe arrays, *Geophys. J. R. Astr. Soc.,* **26**, 99-109. (Unclassified)

McKisic, J. M. (1997), "Infrasound and the Infrasonic Monitoring of Atmospheric Nuclear Explosions," Tracor Applied Sciences final report to Phillips Laboratory, PL-TR-97-2123, February. (Unclassified)

McLaughlin, K.L., B. Shkoller, D.E. Wilkins, and T.G. Barker (1997), Advances in numerical methods, Maxwell Technologies Report MFD-TR-97-15870. (Unclassified)

Pierce, A. D. and J. W. Posey (1971), "Theory of the Excitation and Propagation of Lamb's Atmospheric Edge Mode from Nuclear Explosions," *Geophys. J. R. astr. Soc.,* **26**, 341-368. (Unclassified)

Posey, J. W. and A. D. Pierce (1971), "Estimation of nuclear explosion energies from microbarograph records," *Nature,* **232**, 253. (Unclassified)

Noel, S.D. and Whitaker, R.W. (1991), Comparison of noise reduction systems, LANL report LA-12008-MS UC-700. (Unclassified)

Schlichting, H. (1960), Boundary layer theory, Publ. McGraw Hill. (Unclassified)

Sereno, T. J., S. R. Bratt, and G. Yee (1990), "NetSim: A computer program for simulating detection and location capability of regional seismic networks," SAIC Annual Technical Report to DARPA, SAIC 90/1163, March. (Unclassified)

Stevens, J.L., D. Adams, G.E. Baker, H. Xu, J. Morris, I. Divnov, V. Bourchik, and I. Kitov, (1999), Infrasound scaling and sttenuation relations from Soviet explosion data and instrument design criteria from experiments and simulations, *Proceedings 21*[th] *Annual Seismic Research Symposium on monitoring a CTBT,* 185-194. (Unclassified)

Stevens, J.L., G.E. Baker, J.R. Murphy, and J. Morris (1998), Infrasound excitation and propagation research, *Proceedings 20th Annual Seismic Research Symposium on monitoring a CTBT.* (Unclassified)

Stull, R (1988), An Introduction to Boundary Layer Meteorology, Publ. Kluwer Acad. Press. Wexler, H. and W. A. Hass (1962), "Global atmospheric pressure effects of the October 30, 1961 explosion," *J. Geophys. Res.*, v. 67, pp. 3875-3887. (Unclassified)

Whitaker, R. W. (1995), "Infrasonic Monitoring," proceedings of the 17th annual Seismic Research Symposium in Scottsdale, AZ, September 12-155, 1995, 997-1000. (Unclassified)

Wilson, R.W., J.V. Olson, and R. Richards (1996), Library of typical infrasound signals, ENSCO Report. (Unclassified)

Appendix A
Time constants of low - (τ_l) and high-pass (τ_h) filters of microbarographs.

Instrument response correction. The microbarograph is a differential manomenter made up of two volumes separated by a diaphragm. The first volume is directly connected to atmosphere, the second one through a high acoustic resistance (capillary tube). The diaphragm's flexure is proportional to δP. This system is an acoustical high-pass filter with time constant:

$$\tau_h = 8\eta LV / \pi r^4 p_0,$$

where η - dynamic viscosity of air, L and r - length and radius of capillary tube, P_0 - average atmospheric pressure. High-frequency ($f \gg 1/2\pi\tau_h$) pressure variations pass such filter with minimal distortion, but low-frequency pressure variations attenuate and lead atmospheric pressure changes in phase.

The amplitude $A_h(f)$ and phase $\varphi_h(f)$ responses of the microbarograph as an acoustical high-pass filter can be written as:

$$A_h = \frac{1}{\sqrt{1+1/(2\pi f \tau_h)^2}}, \qquad \varphi_h = \text{arctg}\,(1 / 2\pi f\,\tau_h).$$

To restrict the frequency band, the microbarographs (except MBS) were equipped with built-in electrical low-pass filters, which attenuate and lag in phase the high frequency signal relative to the input signal, but allows to pass low ($f \ll 1/2\pi\tau_l$) frequencies. Amplitude A_l and phase φ_l responses of the low-pass filter are:

$$A_l = \frac{1}{\sqrt{1+(2\pi f \tau_1)^2}}, \qquad \varphi_l = -\,\text{arctg}\,(2\pi f\,\tau_l).$$

The resulting responses are defined from (2) and (3) as:

$A = A_h \times A_l$, $\varphi = \varphi_h + \varphi_l$, $\bar{A} = A \cdot e^{j\varphi}$,   j - imaginary unit.

Time constants τ_h and τ_l are listed in the table below for each station, and are listed for each waveform in appendix B.

Station No	Name	Device type	τ_l , s	τ_h , s	Records' number[1]	In all on this station[1]
1	Dubna	MBS LMB-P	0 15.0	32.2 1.2	2 3	5
2	Kirov	MBS MBS LMB-58 LMB-P	0 0 1.79 15.0	38.2 32.2 29.3 1.2	13 5 15 13	46
3	Esheri	MBS[2] MBS LMB-58	2.91 0 1.92	36.2 26.3 25.7	6 1 10	17
4	Podolsk	MBS LMB-58 LMB-58	0 2.0 1.8	32.2 28.4 29.9	4 10 2	16
5	Oussouriysk	LMB-58 MBL MBB	2.2 10.6 0	16.6 16.4 16.6	15 11 12	38
6	Petropavlovsk-Kamchatskiy	LMB-58 IMB	1.78 12.2	22.7 5.9	12 15	27
7	Yuzhno-Sakhalinsk	MBS LMB-58	0 9.0	32.2 28.5	15 17	32
8	Zhvanets	MBS MBS LMB-58 LMB-58	0 0 1.7 1.3	32.2 32.2 23.8 32.3	10 7 3 4	24
9	Mayly-Say	LMB-58 LMB-P	4.2 1.2	37.0 15.0	19 12	31
10	Semipalatinsk	MBS LMB-58 MB-10	0 1.6 1.8	32.21 25.3 17.2	5 11 11	27
11	Baykal region	IMB	12.2	5.9	6	6
12	Olenegorsk	MBS	0	30.8	2	2
13	Kooldoor	EDMB-I EDMB-II	0 0	180 180	3 3	6
14	Kazakhstan	MBS	0	28.4	5	5
15	Kap. Yar	MBS	0	33.0	5	5
16	Yeniseysk	MBS	0	29.4	17	17
17	Leningrad reg.	MBS	0	34.2	3	3

[1] - total number of records, prepared to digitization and processing.
[2] - with noise-reducing arrangement.

Appendix B
Waveform Parameters and IDG Measurements

Notation and Definitions:

- t - time;
- f - frequency, [Hz];
- $\omega = 2\pi f$ - angular frequency, [rad/s];
- P(t) - examined signal and noise summarized pressure, [Pa];
- $P_N(t)$ - noise pressure, [Pa];
- $P_S(t) = P(t) - P_N(t)$ - signal pressure, [Pa];
- T - duration of analyzed record's segment, [s];
- T_1 - period of signal's first arrival;
- T_c - period of oscillation with maximal amplitude after first arrival;
- $I(t) = \int_0^t P(t)dt$ - pressure specific impulse, [Pa·s];
- $E(t) = (1/\rho c)\cdot\int_0^t P^2(t)dt$ - surface density of acoustic disturbance energy, [J/m²], where ρ и c - air density and sound speed in atmosphere at the earth surface (it is taken ρc = 426-kg/m²·s);
- N_F - points number for FFT;
- f_m - maximum frequency in interval [0; f_m], contained 90% of energy of examined record's length;

Waveform	q, KT	R, km	R/q^{1/3}	St. #	Azim., deg.	Instrum. Resp. Type	T_h, s	T_1, s	NOISE W, W/m²	P_N, Pa	f_{0.9}, Hz	E_N, J/m²	SIGNAL P_1, Pa	P_m, Pa	f_{0.9}, Hz	E_S, J/m²	T_1, s	T_c, s
9/4/61						HOB = 725 m								Mean f_{0.9}	3.80E-01			
088A4101	9	1140	548	9	203.9	LMB-58	37	4.2	1.27E-04	0.233	1.35E-01	1.13E-01	0.7	2.6	3.50E-01	2.78E-01		10.00
088A4102	9	2100	1010	2	307.9	LMB-P	15	1.2	5.14E-03	1.480	2.80E-01	4.58E+00	10	13.5	4.10E-01	3.82E+00	21.00	12.00
9/5/61						HOB = 500 m								Mean f_{0.9}	1.54E-01			
089A3901	16	1140	452	9	203.9	LMB-58	37	4.2	2.11E-04	0.300	1.20E-01	1.92E-01	2.1	3.2	3.00E-01	2.87E-01	26.00	15.00
089A3902	16	2100	833	2	307.9	LMB-P	15	1.2	1.98E-06	0.029	6.50E-02	2.00E-03	0.48	1.1	7.70E-02	4.90E-02	25.00	19.00
089A3903	16	2100	833	2	307.9	LMB-58	29.3	1.79	1.35E-05	0.076	5.20E-02	1.25E-02	1	1.5	8.50E-02	8.70E-02	25.00	17.00
9/6/61						HOB = 22700 m								Mean f_{0.9}	1.52E-01			
091A6101	11	800	360	3	211	LMB-58	25.7	1.92	6.25E-05	0.163	3.00E-01	5.61E-02	2.5	5.7	1.16E-01	2.99E-01	20.00	10.00
091A6102	11	900	405	4	323.7	LMB-58	28.4	2	3.84E-04	0.404	7.50E-02	3.44E-01	3.5	8	1.17E-01	2.66E+00	32.00	13.00
091A6103	11	900	405	4	323.7	LMB-58	29.9	1.8	5.32E-04	0.476	3.30E-01	4.78E-01	3	7.5	3.70E-01	1.79E+00	26.00	11.00

091A6104	11	900	405	4	323.7	MBS	32.2	0	3.22E-05	0.117	6.30E-02	2.90E-02	0.8	1.4	8.20E-02	2.10E-02	30.00	13.00
091A6105	11	1100	495	2	12.2	LMB-58	29.3	1.79	3.88E-04	0.407	8.50E-02	3.45E-01	3.4	5	1.25E-01	9.10E-01	25.00	11.00
091A6106	11	1400	630	8	274.2	MBS	32.2	0	1.72E-05	0.086	0,1	1.53E-02	0.8	2	1.02E-01	1.47E-01	26.00	12.00
9/10/61																		
					HOB = 2000 m									Mean f$_{0.9}$	1.95E-02			
095A0001	2700	2200	158	4	210.2	LMB-58	28.4	2	1.86E-03	0.890	6.20E-02	1.61E+00	8	13	3.30E-02	1.58E+01	215.00	45.00
095A0002	2700	2200	158	4	210.2	LMB-58	29.3	1.8	1.48E-03	0.794	5.80E-02	1.29E+00	7	11.5	3.60E-02	1.10E+01	200.00	43.00
095A0003	2700	2200	158	1	211.1	MBS	32.2	0	1.50E-03	0.799	3.90E-02	2.55E+00	9	13	1.70E-02	2.39E+01	160.00	60.00
095A0004	2700	2200	158	1	211.1	LMB-P	15	1.2	9.07E-04	0.622	2.40E-02	1.61E+00	12.5	13.2	1.45E-02	2.72E+01	180.00	45.00
095A0005	2700	2350	169	16	115.6	MBS	29.4	0	6.12E-04	0.511	4.70E-02	3.70E-01	17.5	36	2.05E-02	1.12E+02	170.00	50.00
095A0006	2700	2850	205	10	139.9	LMB-58	25.3	1.6	4.64E-03	1.406	9.50E-03	4.13E+00	3.5	12.2	1.40E-02	1.22E+01	175.00	45.00
095A0007	2700	2850	205	10	139.9	MBS	32.2	0	1.02E-03	0.659	1.70E-02	9.90E-01	3.3	10.8	1.45E-02	1.10E+01	210.00	85.00
095A0008	2700	3150	226	8	221.6	MBS	32.2	0	8.63E-04	0.606	1.50E-02	7.70E-01	10.3	14.5	1.25E-02	2.14E+01	220.00	80.00
095A0009	2700	3150	226	8	221.6	LMB-58	32.3	1.3	4.28E-04	0.427	1.50E-02	3.80E-01	4	7.2	1.30E-02	4.95E+00	250.00	95.00
095A0010	2700	3150	226	8	221.6	MBS	32.2	0	6.13E-04	0.511	7.00E-02	5.50E-01	3.2	8.5	1.60E-02	1.02E+01	200.00	80.00
095A0011	2700	2800	201	15	193.4	MBS	33	0	1.29E-03	0.741	3.50E-02	7.80E-01		12.2	1.85E-02	8.30E-01	220.00	80.00
095A0012	2700	3500	251	3	199.2	LMB-58	25.7	1.92	3.45E-04	0.383	2.57E-02	2.10E-01	4.5	8	3.70E-02	4.73E+00	180.00	70.00
095A0013	2700	3500	251	3	199.2	MBS	36.2	2.91	6.08E-05	0.161	4.10E-03	3.67E-02	7.6	9.3	1.60E-02	9.88E-02	200.00	65.00
095A0014	2700	3800	273	9	154.7	LMB-58	37	4.2	1.67E-04	0.267	4.80E-02	1.40E-01	7	17	2.40E-02	3.63E+01	160.00	80.00
095A0015	2700	4850	348	6	57.5	IMB	12.2	5.9	2.33E-03	0.996	1.22E-02	1.99E+00	18	8	1.22E-02	2.82E+01	240.00	60.00
095A0016	2700	4850	348	6	57.5	LMB-58	22.7	1.78	8.37E-04	0.597	1.22E-02	7.40E-01	2	9	1.73E-02	1.98E+01	220.00	70.00
095A0017	2700	5000	359	5	86	MBL	16.4	10.6	1.30E-02	2.353	5.20E-03	1.16E+01	8.5	14	1.70E-02	6.95E+00	210.00	75.00
095A0018	2700	5000	359	7	74.4	MBS	32.2	0	4.75E-04	0.450	5.60E-03	4.20E-01	7	16	2.10E-02	2.44E+01	215.00	65.00
095A0019	2700	5000	359	7	74.4	LMB-58	28.5	9	6.80E-04	0.538	7.50E-03	6.10E-01	6	19	2.05E-02	4.06E+01	220.00	60.00
095A0020	2700	1700	122	2	189.3	LMB-58	29.3	1.79	2.63E-04	0.335	1.25E-02	2.30E-01	16	21	2.05E-02	2.47E+01	195.00	60.00
095A0021	2700	1700	122	2	189.3	MBS	32.2	0	3.14E-04	0.366	2.10E-02	2.70E-01	23	22	1.65E-02	4.94E+01	160.00	50.00
095A0022	2700	1700	122	2	189.3	MBS	38.2	0	2.46E-03	1.024	2.13E-02	2.10E+00	21.5	21	1.60E-02	1.63E+02	130.00	40.00
095A0023	2700	1700	122	2	189.3	LMB-P	15	1.2	1.02E-04	0.208	3.40E-02	8.80E-02	12.5	25	2.08E-02	3.31E+01	170.00	50.00
9/12/61																		
					HOB = 1190 m									Mean f$_{0.9}$	2.09E-02			
099A2001	1150	1700	162	2	189.3	LMB-58	29.3	1.79	2.31E-03	0.992	1.73E-02	2.06E+00	4.4	11.6	2.57E-02	5.57E+00	180.00	45.00
099A2002	1150	1700	162	2	189.3	MBS	32.2	0	1.00E-03	0.653	2.80E-02	8.90E-01	2.8	6.8	2.51E-02	3.30E+00	170.00	43.00
099A2003	1150	1700	162	2	189.3	MBS	38.2	0	1.57E-02	2.586	3.25E-02	1.40E+01	2.6	8.8	2.25E-02	1.04E+01	150.00	55.00
099A2004	1150	1700	162	2	189.3	LMB-P	15	1.2	1.12E-03	0.691	2.25E-02	9.90E-01	2	6.8	2.37E-02	2.40E+01	165.00	46.00
099A2005	1150	2200	210	4	210.2	LMB-58	28.4	2	1.92E-04	0.286	1.80E-02	1.71E-01		2.2	2.12E-02	8.90E-01	180.00	70.00
099A2006	1150	2200	210	1	211.1	LMB-P	15	1.2	3.19E-04	0.369	2.30E-02	2.80E-01	1.8	3.8	3.07E-02	1.83E+00	180.00	35.00
099A2007	1150	2200	210	1	211.1	MBS	32.2	0	6.07E-06	0.051	1.40E-02	5.40E-03	0.6	2.1	2.87E-02	4.30E-01	195.00	43.00
099A2008	1150	2350	224	16	115.6	MBS	29.4	0	1.74E-04	0.272	6.50E-03	4.20E-01	3.7	6.4	2.80E-02	2.91E+00	135.00	48.00

099A2009	1150	2850	272	10	139.9	MB-10	17.2	1.8	5.58E-02	4.876	4.00E-03	4.96E+01	11	37	1.90E-02	2.75E+01	210.00	60.00
099A2010	1150	2850	272	10	139.9	LMB-58	25.3	1.6	2.66E-03	1.064	1.90E-02	2.36E+00	2.8	38	2.52E-02	8.94E+01	205.00	80.00
099A2011	1150	3150	301	8	221.6	MBS	32.2	0	1.68E-04	0.268	3.60E-02	1.50E-01	2.2	6.8	1.45E-02	1.16E+01	260.00	95.00
099A2012	1150	3150	301	8	221.6	MBS	32.2	0	1.76E-02	2.738	6.50E-03	1.57E+01	4.8	5.5	1.50E-02	0.00E+00		
099A2013	1150	3150	301	8	221.6	LMB-58	32.3	1.3	8.34E-03	1.885	1.07E-02	7.42E+00	1.2	8.8	1.40E-02	4.73E+00	160.00	65.00
099A2014	1150	2950	282	14	165.9	MBS	28.4	0	5.01E-05	0.146	5.80E-03	4.50E-02	1.9	3.1	2.10E-02	7.32E-01	170.00	64.00
099A2015	1150	3500	334	3	199.2	LMB-58	25.7	1.9	1.69E-04	0.268	5.30E-02	1.50E-01	2.1	3.9	2.10E-02	1.62E+00	195.00	40.00
099A2016	1150	3500	334	3	199.2	MBS	36.2	2.9	2.38E-03	1.007	4.80E-03	2.12E+00	2	4.2	2.40E-02	3.72E-01	150.00	77.00
099A2017	1150	4850	463	6	57.5	IMB	12.2	5.9	7.17E-04	0.553	5.00E-03	6.40E-01	7	4.5	1.35E-02	3.30E+00	210.00	65.00
099A2018	1150	5000	477	5	86	MBB	16.6	0	2.16E-03	0.959	6.00E-03	1.92E+00	8	11.6	1.60E-02	1.78E+01	165.00	57.00
099A2019	1150	5000	477	5	86	MBL	16.4	10.6	4.26E-03	1.347	4.70E-03	3.79E+00	8.2	14.3	1.95E-02	1.79E+01	220.00	55.00
099A2020	1150	5000	477	5	86	LMB-58	16.6	2.2	7.56E-04	0.567	1.00E-02	6.70E-01		8.8	1.80E-02	9.53E+00	220.00	51.00
099A2021	1150	5000	477	7	74.4	LMB-58	28.5	9	2.48E-03	1.028	2.75E-02	2.20E+00	4.6	9.4	1.85E-02	7.38E+00	210.00	59.00
099A2022	1150	3800	363	9	154.7	LMB-58	37	4.2	2.15E-04	0.303	9.00E-03	1.90E-01		13	2.30E-02	1.46E+01	195.00	60.00
099A2023	1150	4850	463	6	57.5	LMB-58	22.7	1.8	2.47E-04	0.324	4.30E-03	2.19E+00	2.1	10.8	1.40E-02	7.18E+00	205.00	77.00
9/14/61					HOB = 1700 m									Mean f$_{0.9}$	2.05E-02			
102A0601	1200	1700	160	2	189.3	LMB-58	29.3	1.79	2.86E-04	0.349	1.90E-02	2.54E-01	7	14.5	2.35E-02	9.70E+00	142.00	40.00
102A0602	1200	1700	160	2	189.3	MBS	32.2	0	2.70E-04	0.339	3.35E-02	2.41E-01	19	35	2.10E-02	7.09E+01	141.70	41.80
102A0603	1200	1700	160	2	189.3	MBS	38.2	0	6.99E-04	0.546	3.05E-02	6.23E-01	8.8	15.7	2.25E-02	4.56E+01	143.00	42.20
102A0604	1200	1700	160	2	189.3	LMB-P	15	1.2	4.98E-05	0.146	3.15E-02	4.40E-02	3.5	9.2	3.15E-02	3.76E+00	133.20	42.60
102A0605	1200	1800	169	17	226.7	MBS	34.2	0	9.06E-05	0.196	9.50E-03	8.10E-02	1.8	5	1.40E-02	2.26E+00	182.40	76.00
102A0606	1200	2950	278	14	165.9	MBS	28.4	0	2.60E-04	0.333	3.40E-02	2.31E-01	2	5.8	2.11E-02	3.28E+00	182.40	60.80
102A0607	1200	2800	263	15	193.4	MBS	33	0	2.41E-04	0.320	1.90E-02	2.14E-01	1.1	2.4	2.15E-02	1.75E-01	187.00	51.30
102A0608	1200	3500	329	3	199.2	MBS	36.2	2.9	5.56E-04	0.487	1.00E-01	4.95E-01	4	5.2	1.80E-02	2.36E+00	185.00	54.30
102A0609	1200	3500	329	3	199.2	LMB-58	29.7	1.9	1.07E-04	0.213	1.80E-02	9.50E-02	2.7	3.2	1.90E-02	1.04E+00	187.00	47.70
102A0610	1200	3800	358	9	154.7	LMB-P	15	1.2	1.40E-03	0.772	1.81E-02	1.24E+00	8.4	13.2	2.00E-02	1.86E+01	179.80	43.60
102A0611	1200	4850	456	6	57.5	LMB-58	29.7	1.8	4.00E-04	0.413	2.47E-02	3.56E-01	5.8	11	3.10E-02	6.95E+00	174.40	54.50
102A0612	1200	4850	456	6	57.5	IMB	12.2	5.9	9.93E-05	0.206	4.50E-02	8.80E-02	4	5.7	2.63E-02	2.85E+00	170.00	47.00
102A0613	1200	5000	471	5	86	LMB-58	16.6	2.2	8.30E-04	0.595	1.70E-02	7.39E-01	1.2	3.7	1.38E-02	1.53E+00	154.00	55.00
102A0614	1200	5000	471	5	86	MBL	16.4	10.6	4.00E-03	1.305	4.00E-03	3.56E+00	5	5	7.00E-03	9.18E-01	178.00	57.00
102A0615	1200	5000	471	5	86	MBB	16.6	0	2.93E-04	0.353	1.00E-02	2.61E-01	4.6	4.6	1.70E-02	3.10E+00	230.00	65.00
102A0616	1200	5000	471	7	74.4	LMB-58	28.5	9	1.33E-03	0.753	1.00E-02	1.19E+00	3.2	10.2	2.25E-02	1.10E+01	147.20	52.70
102A0617	1200	5000	471	7	74.4	MBS	32.2	0	8.70E-04	0.609	5.20E-03	7.75E-01	2.5	5.2	1.90E-02	4.75E+00	152.60	47.20
9/14/61					HOB = 0.5 m									Mean f$_{0.9}$	7.20E-02			
103A3801	0.4	1140	1547	9	203.9	LMB-58	37	4.2	1.38E-04	0.242	5.20E-02	1.23E-01		0.9	7.20E-02	1.24E-01		12.00
9/20/61					HOB = 1600 m								2.2	Mean f$_{0.9}$	3.18E-02			

111A0301	450	2300	300	16	115.6	MBS	29.4	0	2.57E-04	0.331	1.90E-02	2.29E-01	1.6	5.4	3.10E-02	9.35E-01	87.00	43.50
111A0302	450	3800	496	9	154.7	LMB-58	37	4.2	3.06E-04	0.361	7.30E-03	1.83E-01	1.2	3.5	2.50E-02	8.93E-01	165.00	45.00
111A0303	450	4850	633	6	57.5	IMB	12.2	5.9	1.36E-03	0.761	8.30E-03	1.21E+00	2	5.9	3.20E-02	1.99E+00	140.00	40.00
111A0304	450	4850	633	6	57.5	LMB-58	22.7	1.78	7.26E-04	0.556	1.60E-02	6.50E-01	2.4	10.8	3.50E-02	2.46E+00	163.50	35.40
111A0305	450	5000	652	7	74.4	LMB-58	28.5	9	5.12E-04	0.467	4.00E-02	4.60E-01	4.4	14.4	3.60E-02	8.30E-01	163.50	36.40
111A0306	450	5000	652	7	74.4	MBS	32.2	0	4.22E-04	0.424	2.90E-02	3.76E-01	4	12.4	3.20E-02	5.64E+00	174.40	40.00
9/21/61						HOB = 110 m								Mean f0,9	1.18E-01		
112A4301	0.8	1100	1185	14	243	MBS	28.4	0	6.80E-05	0.170	4.00E-02	6.10E-02	0.6	2.7	1.15E-01	6.80E-02	12.00	10.00
112A4302	0.8	1140	1228	9	203.9	LMB-58	37	4.2	8.87E-06	0.061	3.00E-01	8.00E-03	0.2	0.8	1.20E-02	2.30E-02	21.00	8.00
9/22/61						HOB = 1300 m								Mean f0,9	3.58E-02		
113A1501	260	2350	368	16	115.6	MBS	29.4	0	1.26E-04	0.231	7.70E-02	1.12E-01	1	2.4	4.90E-02	2.24E-01		37.30
113A1502	260	5000	783	5	86	LMB-58	16.6	2.2	5.35E-04	0.478	1.00E-02	4.77E-01	1.5	2.9	3.10E-02	2.52E-01	66.70	40.00
113A1503	260	5000	783	5	86	MBB	16.6	0	3.10E-05	0.115	3.50E-02	2.78E-02	1	2	2.70E-02	5.61E-01	80.00	30.00
113A1504	260	5000	783	7	74.4	LMB-58	28.5	9	2.30E-03	0.990	8.20E-03	2.05E+00	2	3.6	3.60E-02	2.24E-01	70.00	27.00
9/26/61						HOB = 665 m				0.000				Mean f0,9	7.75E-02		
114A4001	1.2	3700	3482	8	287.1	MBS	32.2	0	8.57E-05	0.191	7.20E-02	7.63E-02	1.8	3	8.00E-02	2.13E-01	19.00	10.00
114A4002	1.2	3700	3482	8	287.1	MBS	32.2	0	5.47E-05	0.153	7.10E-02	4.87E-02	1.2	1.6	7.50E-02	1.34E-01	24.00	14.00
10/2/61						HOB = 1500 m								Mean f0,9	4.65E-02		
116A2101	250	2200	349	1	211.1	LMB-P	15	1.2	9.07E-07	0.020	2.53E-02	8.00E-04	0.8	1.3	4.60E-02	1.38E-01	110.00	43.00
116A2102	250	2350	373	16	115.6	MBS	29.4	0	1.83E-04	0.279	8.30E-02	1.10E-01	0.9	6.3	6.20E-02	7.13E-01		20.90
116A2103	250	2850	452	10	139.9	MBS	32.2	0	1.01E-04	0.208	9.80E-02	2.30E-02	1.2	4.2	9.30E-02	5.63E-01		18.20
116A2104	250	2850	452	10	139.9	LMB-58	25.3	1.6	5.24E-04	0.472	1.40E-02	4.71E-01	0.8	2.2	4.50E-02	1.95E+00		20.00
116A2105	250	2850	452	10	139.9	MB-10	17.2	1.8	3.00E-04	0.357	2.40E-02	2.69E-01	0.4	1.75	2.40E-02	2.27E-01		41.20
116A2106	250	3800	603	9	154.7	LMB-58	37	4.2	1.70E-04	0.269	6.50E-02	1.51E-01	0.9	2	4.80E-02	3.50E-01		34.80
116A2107	250	4850	770	6	57.5	LMB-58	22.7	1.78	2.74E-05	0.108	3.30E-02	2.40E-02	1.3	4.6	4.40E-02	1.23E+00	115.50	34.80
116A2108	250	4850	770	6	57.5	IMB	12.2	5.9	2.70E-04	0.339	5.40E-03	2.45E-01	0.9	3.1	4.90E-02	4.96E-01	130.00	37.00
116A2109	250	5000	794	5	86	LMB-58	16.6	2.2	2.38E-04	0.318	1.75E-02	2.15E-01	0.8	2	4.50E-02	1.12E-01	88.00	20.80
116A2110	250	5000	794	5	86	MBB	16.6	0	3.50E-05	0.122	1.40E-02	3.20E-02	0.8	2.2	4.50E-02	2.42E-01	113.00	22.00
116A2111	250	5000	794	5	86	MBL	16.4	10.6	1.03E-04	0.209	4.00E-02	9.30E-02	0.9	4.2	4.90E-02	4.73E-01	120.00	22.00
116A2112	250	5000	794	7	74.4	MBS	32.2	0	4.61E-04	0.443	3.10E-02	4.17E-01	1.6	2.4	3.50E-02	4.76E-01		38.90
116A2113	250	5000	794	7	74.4	LMB-58	25.3	1.6	1.57E-03	0.817	8.30E-02	1.42E+00	3.2	4	4.60E-02	1.15E+00		
10/4/61						HOB = 605 m								Mean f0.9	1.35E-01		
117A4401	13	1300	553	16	40.1	MBS	29.4	0	4.92E-05	0.145	1.00E-01	4.37E-02	0.4	2.5	1.35E-01	1.58E-01		
10/6/61						HOB = 41300 m								Mean f0.9	5.28E-02		
119A6301	40	900	263	4	323.7	MBS	32	0	3.06E-06	0.036	6.05E-02	2.72E-03	0.28	1.36	6.50E-02	4.78E-02	53.00	30.00
119A6302	40	900	263	4	323.7	LMB-58	28.4	2	4.01E-06	0.041	7.80E-02	3.57E-03	0.32	2.1	5.00E-02	1.65E-01	48.00	31.00

ID																			
119A6303	40	40	1100	322	2	12.2	MBS	32.2	0	2.28E-03	0.986	6.50E-02	2.03E+00	2	9.2	4.60E-02	2.19E+00		30.00
119A6304	40	40	1100	322	2	12.2	LMB-P	15	1.2	3.16E-04	0.367	5.50E-02	2.82E-01	1.8	7	5.00E-02	9.52E-01	40.00	25.00
10/6/61						HOB = 2700 m								Mean f0.9		1.74E-02			
120A1401		4000	1700	107	2	189.3	MBS	38.2	0	5.53E-03	1.534	4.50E-02	4.92E+00	0.6	7.6	4.65E-02	3.35E+00	70.90	38.00
120A1402		4000	1700	107	2	189.3	LMB-58	29.3	1.79	1.14E-03	0.697	2.90E-02	1.02E+00	1.4	8.5	2.75E-02	2.58E+00		40.90
120A1403		4000	1850	117	17	228	MBS	34.2	0	2.45E-04	0.323	3.70E-02	2.18E-01	4.4	12.8	1.10E-02	2.36E+01	136.20	109.00
120A1404		4000	2200	139	4	210.2	LMB-58	28.4	2	6.57E-05	0.167	1.60E-02	5.80E-02	3	7.4	8.50E-03	4.41E+00	272.50	122.60
120A1405		4000	2200	139	4	210.2	MBS	32.2	0	5.95E-05	0.159	4.60E-02	5.30E-02	1	2.4	9.00E-03	3.37E-01	294.30	120.00
120A1406		4000	2350	148	16	115.6	MBS	29.4	0	2.17E-04	0.304	6.50E-03	1.93E-01	3.4	5	2.30E-02	1.51E+00	226.20	63.10
120A1407		4000	2850	180	10	139.9	LMB-58	25.3	1.6	6.67E-03	1.686	5.40E-02	5.94E+00		11.6	4.60E-02	4.06E+00	163.50	54.50
120A1408		4000	2850	180	10	139.9	MB-10	17.2	1.8	6.26E-03	1.633	5.50E-02	5.58E+00		21	1.40E-02	2.70E+01	207.10	65.40
120A1409		4000	3150	198	8	221.6	LMB-58	32.3	1.3	1.05E-03	0.668	3.60E-02	9.32E-01		4.6	1.00E-02	1.96E+00		105.00
120A1410		4000	3150	198	8	221.6	MBS	32.3	0	8.45E-06	0.060	3.70E-02	8.00E-03	0.7	1.15	9.30E-03	1.27E-01	250.70	114.50
120A1411		4000	3500	220	3	199.2	LMB-58	25.7	1.92	2.44E-04	0.322	5.00E-02	2.17E-01	3.4	7.2	1.10E-02	3.31E+00	250.70	136.20
120A1412		4000	3500	220	3	199.2	MBS	36.2	2.91	3.30E-03	1.186	5.00E-02	2.94E+00	3	5.8	7.00E-03	1.13E+00		
120A1413		4000	3800	239	9	154.7	LMB-P	15	1.2	1.94E-02	2.878	1.10E-02	1.73E+01	18	19	7.00E-03	4.13E+01	294.30	65.40
120A1414		4000	4850	306	6	57.5	LMB-58	22.7	1.78	2.32E-04	0.315	5.80E-02	2.07E-02	4	4.2	1.10E-02	2.36E+00	272.50	56.30
120A1415		4000	4850	306	6	57.5	IMB	12.2	5.9	6.70E-04	0.534	4.20E-03	5.97E-01	13.5	22	2.05E-02	4.63E+01	360.00	40.00
120A1416		4000	5000	315	5	86	LMB-58	16.6	2.2	6.17E-04	0.513	3.70E-02	5.50E-01	2	7.6	1.70E-02	4.04E+00		72.70
120A1417		4000	5000	315	5	86	MBB	16.6	0	1.78E-03	0.871	1.60E-02	1.58E+00	2	8.5	1.63E-02	5.10E+00	234.00	58.00
120A1418		4000	5000	315	5	86	MBL	16.4	10.6	5.45E-03	1.524	8.00E-03	4.86E+00	2.2	9.2	1.13E-02	4.05E+00	185.00	62.00
120A1419		4000	5000	315	7	74.4	LMB-58	28.5	9	8.50E-04	0.602	6.20E-02	7.57E-01	9	20.5	2.50E-02	3.06E+01	218.00	52.70
120A1420		4000	5000	315	7	74.4	MBS	32.2	0	2.34E-03	0.999	1.20E-02	2.09E+00	14	20	1.80E-02	4.88E+01	218.00	54.50
10/17/61						HOB = 505 m					0.000			Mean f0.9		1.83E-01			
123A4501		6.6	1140	608	9	203.9	LMB-58	37	4.2	1.90E-04	0.284	8.00E-02	1.69E-01	1	1.8	6.50E-02	2.50E-02	28.00	13.00
123A4502		6.6	1300	693	16	40.1	MBS	29.4	0	1.46E-05	0.079	1.80E-01	1.30E-02	1.5	5	3.00E-01	1.90E-01	20.00	10.00
10/19/61						HOB = 710 m								Mean f0.9		1.20E-01			
124A4601		10	1140	529	9	203.9	LMB-58	37	4.2	9.01E-05	0.196	1.25E-01	8.00E-02	1.8	2.9	1.10E-01	2.93E-01	30.00	10.00
124A4602		10	1300	603	16	40.1	MBS	29.4	0	6.64E-06	0.053	1.45E-01	6.00E-03	0.4	7.6	1.30E-01	6.10E-01	18.00	12.00
10/20/61						HOB =	m							Mean f0.9		2.38E-02			
125A0201		1450	1700	150	2	189.3	MBS	32.2	0	7.46E-04	0.564	3.00E-02	6.47E-01	3.3	5.9	9.00E-03	2.25E+00	142.00	97.00
125A0202		1450	1700	150	2	189.3	LMB-P	15	1.2	2.47E-04	0.324	3.26E-02	2.20E-01	2.5	9.3	2.13E-02	7.54E+00	139.00	53.00
125A0203		1450	1700	150	2	189.3	LMB-58	29.3	1.79	1.04E-04	0.210	3.00E-02	9.00E-02	2.5	4.5	1.20E-02	1.71E+00	165.00	78.00
125A0204		1450	2350	208	16	115.6	MBS	29.4	0	4.63E-05	0.140	1.10E-02	2.60E-02	2.2	4.2	3.70E-02	1.15E+00	165.00	40.00
125A0205		1450	2850	252	10	139.9	MBS	32.2	0	1.75E-04	0.273	3.00E-02	7.50E-02	6	14.3	2.40E-02	8.53E+00	155.00	51.00
125A0206		1450	2850	252	10	139.9	LMB-58	25.3	1.6	5.51E-03	1.532	5.00E-03	4.86E+00	4.2	14	2.40E-02	7.63E+00	155.00	53.00

ID																	
125A0207	1450	2850	252	10	139.9	MB-10	17.2	1.8	9.27E-03	1.988	6.50E-03	8.19E+00	4	13.5	2.40E-02	7.40E+00	170.00	56.00
125A0208	1450	2800	247	15	193.4	MBS	28.4	0	1.00E-04	0.206	1.60E-02	9.00E-03	2	4.8	6.00E-03	9.94E-01		150.00
125A0209	1450	3450	305	11	104.8	IMB	12.2	5.9	8.40E-03	1.892	4.70E-02	7.42E+00	13.5	13	1.85E-02	2.73E+01	184.00	62.00
125A0210	1450	3800	336	9	154.7	LMB-58	37	4.2	8.58E-04	0.605	9.00E-03	7.58E-01	2.2	11.2	3.10E-02	5.79E+00	200.00	47.00
125A0211	1450	4850	429	6	57.5	IMB	12.2	5.9	5.68E-03	1.556	5.80E-02	5.01E+00	7.5	10.7	3.90E-02	7.83E+00	200.00	55.00
125A0212	1450	4850	429	6	57.5	LMB-58	22.7	1.78	2.21E-03	0.970	4.10E-02	1.95E+00	6.5	13	2.60E-02	8.10E+00	180.00	47.00
125A0213	1450	5000	442	5	86	MBL	16.4	10.6	2.41E-04	0.321	5.00E-03	2.10E-01	1	3.1	3.30E-02	6.53E-01	180.00	50.00
125A0214	1450	5000	442	5	86	LMB-58	16.6	2.2	9.47E-03	2.008	1.10E-02	8.43E+00	7.5	27	2.60E-02	6.67E+01	185.00	50.00
125A0215	1450	5000	442	5	86	MBB	16.6	0	2.48E-02	3.250	5.60E-02	2.21E+01	5	34	2.75E-02	8.60E+01	190.00	49.00
125A0216	1450	5000	442	7	74.4	MBS	32.2	0	1.36E-03	0.760	1.80E-02	1.21E+00	4	9.5	2.40E-02	8.83E+00	190.00	40.00
125A0217	1450	5000	442	7	74.4	LMB-58	28.5	9	3.69E-03	1.254	5.00E-03	3.23E+00	3	8.8	2.20E-02	6.11E+00	185.00	46.00
10/23/61					HOB = 3500 m									Mean f0.9	6.09E-03		
126A1801	12500	1700	73	2	189.3	LMB-58	29.3	1.79	3.67E-03	1.250	5.80E-03	3.27E+00	19.5	10	3.90E-03	6.80E+01	330.00	
126A1802	12500	1700	73	2	189.3	LMB-P	15	1.2	4.05E-03	1.314	2.80E-02	3.61E+00	29	15	4.50E-03	9.85E+01	310.00	
126A1803	12500	1700	73	2	189.3	MBS	32.2	0	3.52E-03	1.224	1.90E-02	3.13E+00	22		4.00E-03	5.04E+01	330.00	
126A1804	12500	1850	80	17	226.7	MBS	34.2	0	1.57E-03	0.817	3.30E-02	1.39E+00	37	9	5.00E-03	1.79E+02	290.00	160.00
126A1805	12500	2200	95	4	210.2	LMB-58	28.4	2	5.66E-04	0.491	1.50E-02	5.00E-01	13	18	4.10E-03	1.82E+02	340.00	155.00
126A1806	12500	2850	123	10	139.9	LMB-58	25.3	1.6	2.45E-02	3.229	1.70E-02	2.18E+01	63	22	8.00E-03	4.82E+02	220.00	120.00
126A1807	12500	2850	123	10	139.9	MB-10	17.2	1.8	1.68E-04	0.268	2.42E-02	1.49E-01	11	6.6	7.10E-03	1.48E+01	200.00	115.00
126A1808	12500	3150	136	8	221.6	MBS	32.2	0	1.63E-02	2.633	2.20E-02	1.45E+01	45	24	4.10E-03	3.16E+02	330.00	190.00
126A1809	12500	3150	136	8	221.6	LMB-58	32.3	1.3	4.91E-03	1.446	3.40E-02	4.37E+00	24	18	4.50E-03	1.27E+02	290.00	210.00
126A1810	12500	3150	136	8	221.6	MBS	32.2	0	7.24E-03	1.756	2.40E-02	6.44E+00	31	21	4.00E-03	1.88E+02	355.00	215.00
126A1811	12500	2800	121	15	193.4	MBS	33	0	6.61E-03	1.678	6.00E-03	5.89E+00	31	12	3.70E-03	1.46E+02	345.00	185.00
126A1812	12500	3500	151	3	199.2	LMB-58	25.7	1.92	2.03E-02	2.941	2.90E-02	1.81E+01	43.5	21	3.90E-03	3.96E+02	370.00	210.00
126A1813	12500	3800	164	9	154.7	LMB-P	15	1.2	3.42E-01	12.072	5.00E-03	3.05E+02	52	40	3.40E-03	1.14E+03	330.00	135.00
126A1814	12500	3800	164	9	154.7	LMB-58	37	4.2	1.57E-02	2.584	1.70E-02	1.40E+01	40	28	4.60E-03	3.72E+02	305.00	130.00
126A1815	12500	4850	209	6	57.5	LMB-58	22.7	1.78	4.89E-02	4.566	4.60E-03	4.36E+01	100	62	8.60E-03	1.24E+02	280.00	180.00
126A1816	12500	4850	209	6	57.5	IMB	12.2	5.9	1.36E-01	7.612	3.30E-03	1.21E+02	90	64	8.00E-03	7.79E+02	310.00	155.00
126A1817	12500	5000	215	5	86	LMB-58	16.6	2.2	1.28E-01	7.376	6.60E-03	1.14E+02	130	92	7.50E-03	3.36E+03	310.00	115.00
126A1818	12500	5000	215	7	74.4	LMB-58	28.5	9	1.44E-03	0.783	2.47E-02	1.28E+00	25	30	1.07E-02	2.45E+02	330.00	105.00
126A1819	12500	5000	215	7	74.4	MBS	32.2	0	1.82E-03	0.881	1.18E-02	1.62E+00	36	32	1.00E-02	3.77E+02	205.00	95.00
126A1820	12500	5000	215	5	86	MBL	16.4	10.6	1.77E-03	0.868	5.80E-03	1.58E+00	25	18	7.80E-03	1.09E+02	275.00	125.00
126A1821	12500	5000	215	5	86	MBB	16.6	0	3.38E-03	1.200	5.00E-03	3.01E+00	14.2	18.5	1.05E-02	6.74E+01	310.00	105.00
10/25/61					HOB = 1450 m					0.000				Mean f0.9	3.18E-02		
128A0901	300	1700	254	2	189.3	LMB-58	29.3	1.79	2.62E-04	0.334	2.70E-02	2.33E-01	2	3.3	2.10E-02	6.81E-01	150.00	51.00
128A0902	300	1700	254	2	189.3	LMB-P	15	1.2	3.12E-04	0.365	3.70E-02	2.78E-01	2.4	4.7	2.70E-02	8.93E-01	136.00	49.00

128A0903	300	2350	351	16	115.6	MBS	29.4	0	4.94E-04	0.459	4.50E-02	4.40E-01		6	4.87E-02	1.70E+00	126.00	45.00
128A0904	300	2850	426	10	139.9	MB-10	17.2	1.8	1.65E-03	0.839	3.80E-02	1.47E+00	1.9	3.2	2.60E-02	4.47E-01	152.00	54.00
128A0905	300	3450	515	11	104.8	IMB	12.2	5.9	1.11E-03	0.688	3.25E-02	9.90E-01	2.2	8.1	3.00E-02	3.05E+00		38.00
128A0906	300	3800	568	9	154.7	LMB-58	37	4.2	7.21E-05	0.175	1.80E-02	6.42E-02	0.8	1.1	3.90E-02	2.20E-01	135.00	52.00
128A0907	300	4850	724	6	57.5	IMB	12.2	5.9	8.44E-04	0.600	7.00E-02	7.51E-01	2.3	3.6	2.25E-02	7.66E-01	145.00	35.00
128A0908	300	4850	724	6	57.5	LMB-58	22.7	1.78	4.78E-04	0.451	3.00E-02	4.26E-01	2.2	5.7	3.80E-02	1.01E+00	143.00	34.00
128A0909	300	5000	747	5	86	LMB-58	16.6	2.2	2.49E-04	0.326	7.50E-03	2.22E-01	2.3	6.8	3.20E-02	3.15E+00	155.00	47.00
128A0910	300	5000	747	5	86	MBB	16.6	0	3.06E-05	0.114	1.60E-02	2.70E-02	0.5	5.1	3.35E-02	7.84E-01	144.00	46.00
10/30/61					HOB = 4000 m									Mean f0.9	5.36E-03			
133A2201	58000	1000	26	12	242.2	MBS	30.8	0	2.66E-03	1.064	2.60E-03	2.36E+00	55	28	4.70E-03	4.03E+02	365.00	180.00
133A2202	58000	1700	44	2	189.3	LMB-58	29.3	1.79	6.52E-04	0.527	7.60E-04	5.81E-01			5.60E-03	2.78E+01	386.00	185.00
133A2203	58000	1700	44	2	189.3	MBS	32.2	0	5.87E-02	5.001	7.50E-03	5.18E+01	150	53	4.80E-03	2.22E+03	393.00	
133A2204	58000	1850	48	17	226.7	MBS	34.2	0	1.01E-02	2.074	8.20E-03	8.96E+00	> 30	34	4.20E-03	6.42E+02	353.00	180.00
133A2205	58000	2200	57	4	210.2	MBS	32.2	0	5.40E-04	0.480	5.70E-03	4.81E-01	24	8.5	4.50E-03	5.90E+01	301.00	190.00
133A2206	58000	2200	57	4	210.2	LMB-58	28.4	2	1.99E-01	9.207	9.00E-03	1.77E+02	>100	>80	4.80E-03	5.90E+03	336.00	205.00
133A2208	58000	2850	74	10	139.9	LMB-58	25.3	1.6	9.57E-02	6.385	1.30E-02	8.12E+01	440	140	7.10E-03	1.85E+04	330.00	126.00
133A2209	58000	2850	74	10	139.9	MB-10	17.2	1.8	1.52E-01	8.047	8.50E-03	1.35E+02	430	90	6.00E-03	1.57E+04	367.00	124.00
133A2210	58000	3150	81	8	221.6	LMB-58	32.3	1.3	1.21E-02	2.270	7.50E-03	1.08E+01	96	36	4.20E-03	1.59E+03	349.00	210.00
133A2211	58000	2950	76	14	165.9	MBS	28.4	0	1.86E-03	0.890	5.50E-03	1.66E+00	42	>23	4.50E-03	2.63E+02	311.00	118.00
133A2212	58000	3450	89	11	104.8	IMB	12.2	5.9	4.48E-02	4.369	5.80E-03	4.00E+01	>13	55		>318		
133A2213	58000	3150	81	8	221.6	MBS	32.2	0	1.92E-03	0.904	5.60E-03	1,71	88	26	4.10E-03	1.31E+03	340.00	200.00
133A2214	58000	3500	90	3	199.2	LMB-58	25.7	1.92	3.15E-02	3.663	8.00E-03	2.80E+01	108	48	5.50E-03	1.98E+03	344.00	150.00
133A2215	58000	3800	98	9	154.7	LMB-P	15	1.2	9.90E-01	20.536	8.20E-03	8.79E+02	380	150	4.20E-03	1.61E+04	323.00	150.00
133A2216	58000	3800	98	9	154.7	LMB-58	37	4.2	4.03E-02	4.143	7.80E-03	3.58E+01	164	88	5.20E-03	2.96E+03	374.00	140.00
133A2217	58000	4850	125	6	57.5	LMB-P	15	1.2	8.15E-02	5.892	1.91E-02	7.26E+01	55	70	6.70E-03	1.50E+03		
133A2218	58000	4850	125	6	57.5	IMB	12.2	5.9	5.83E-02	4.984	1.91E-02	5.19E+01	42	74	3.40E-03	5.02E+02		
133A2219	58000	5000	129	5	86	LMB-58	16.6	2.2	1.83E-01	8.829	3.10E-03	1.63E+02	>95	>50	7.00E-03	4.68E+03	340.00	
133A2220	58000	5000	129	7	74.4	LMB-58	28.5	9	3.40E-02	3.806	6.20E-03	3.03E+01	75	32	8.20E-03	9.49E+02	290.00	
133A2221	58000	5000	129	7	74.4	MBS	32.2	0	2.40E-03	1.011	1.10E-02	2.14E+00	210	160	7.10E-03	7.89E+03	280.00	122.00
11/4/61					HOB = 1750 m									Mean f0.9	1.78E-02			
147A1901	1500	1700	149	2	189.3	LMB-58	29.3	1.79	3.30E-04	0.375	2.00E-02	2.94E-01	4.1	7	1.15E-02	5.04E+00	220.00	98.00
147A1902	1500	1700	149	2	189.3	MBS	32.2	0	1.05E-03	0.669	4.90E-02	9.34E-01	3.8	6.6	1.45E-02	3.26E+00	225.00	102.00
147A1903	1500	1700	149	2	189.3	LMB-P	15	1.2	2.29E-04	0.312	4.70E-02	2.04E-01	2.8	8.8	1.78E-02	4.82E+00	220.00	100.00
147A1904	1500	1850	162	17	226.7	MBS	34.2	0	3.68E-03	1.252	7.60E-02	3.28E+00	3.8	12.4	1.35E-02	7.19E+00		95.00
147A1905	1500	2200	192	4	210.2	LMB-58	28.4	2	1.69E-02	2.683	6.50E-02	1.50E+01		15.2	1.10E-02	1.68E+00		90.00

147A1906	1500	2350	205	16	115.6	MBS	29.4	0	3.15E-04	0.366	5.70E-02	2.80E-01	3.5	6.6	3.15E-02	2.00E+00	140.00	60.00
147A1907	1500	2850	249	10	139.9	LMB-58	25.3	1.6	1.30E-02	2.353	5.80E-02	9.18E+00	5.6	16.4	2.20E-02	6.58E+00		85.00
147A1908	1500	3150	275	8	221.6	MBS	32.2	0	4.17E-04	0.421	5.10E-02	3.71E-01	3.7	7.6	9.00E-03	3.12E+00	240.00	105.00
147A1909	1500	3150	275	8	221.6	MBS	32.2	0	5.05E-04	0.464	5.10E-02	4.50E-01	2.6	6.6	1.12E-02	1.48E+00	230.00	108.00
147A1910	1500	3450	301	11	104.8	IMB	12.2	5.9	1.09E-03	0.681	2.50E-02	9.70E-01	9.7	9.8	1.40E-02	7.03E+00	205.00	
147A1911	1500	3500	306	3	199.2	LMB-58	25.7	1.92	2.28E-03	0.986	4.15E-02	2.03E+00	4	8.4	1.60E-02	3.46E+00	205.00	78.00
147A1912	1500	3500	306	3	199.2	MBS	26.3	0	2.90E-03	1.111	1.57E-02	2.58E+00	4.2	6.8	1.60E-02	2.63E+00	195.00	85.00
147A1913	1500	3800	332	9	154.7	LMB-58	37	4.2	4.13E-04	0.419	4.00E-02	3.70E-01	3.8	7	8.10E-03	3.22E+00	240.00	84.00
147A1914	1500	3800	332	9	154.7	LMB-P	15	1.2	1.15E-03	0.700	1.30E-02	1.03E+00	3.5	10.3	6.00E-03	8.66E+00	250.00	70.00
147A1915	1500	4850	424	6	57.5	IMB	12.2	5.9	6.66E-04	0.533	5.05E-03	5.93E-01	4.7	8.5	3.60E-02	5.18E+00	140.00	58.00
147A1916	1500	4850	424	6	57.5	LMB-58	22.7	1.78	1.06E-03	0.672	4.70E-02	9.43E-01	8	15.4	3.35E-02	1.85E+01	165.00	50.00
147A1917	1500	5000	437	5	86	LMB-58	16.6	2.2	7.60E-04	0.569	6.50E-02	6.76E-01	3.6	10.3	1.90E-02	1.84E+01	190.00	61.00
147A1918	1500	5000	437	5	86	MBL	16.4	10.6	1.45E-04	0.249	4.00E-03	1.29E-01	2.4	2.6	2.35E-02	1.13E+00	200.00	59.00
147A1919	1500	5000	437	7	74.4	LMB-58	28.5	9	1.99E-04	0.291	3.80E-02	1.77E-01	3.6	10.6	2.65E-02	9.90E+00	205.00	82.00
147A1920	1500	5000	437	7	74.4	MBS	32.2	0	4.74E-04	0.449	8.00E-03	4.22E-01	5.2	13.2	1.50E-02	1.43E+01	195.00	85.00

DEPARTMENT OF DEFENSE

DEFENSE TECHNICAL
INFORMATION CENTER
8725 JOHN J. KINGMAN ROAD,
SUITE 0944
FT. BELVOIR, VA 22060-6201
2 CYS ATTN: DTIC/OCA

DEPARTMENT OF DEFENSE
CONTRACTORS

ITT INDUSTRIES
ITT SYSTEMS CORPORATION
1680 TEXAS STREET, SE
KIRTLAND AFB, NM 87117-5669
2 CYS ATTN: DTRIAC
       ATTN: DARE

TITAN PULSE SCIENCES DIVISION
2700 MERCED ST.
SAN LEANDRO, CA 94577-0599
       ATTN: J. STEVENS